

1

2

3 **Glutathione binding to the plant *AtAtm3* transporter and implications for the**
4 **conformational coupling of ABC transporters**

5

6 Chengcheng Fan^{1,2} and Douglas C. Rees^{1,*}

7 ¹Division of Chemistry and Chemical Engineering, Howard Hughes Medical Institute, California
8 Institute of Technology, Pasadena, CA 91125

9 ²Present address: Division of Biology and Biological Engineering, California Institute of
10 Technology, Pasadena, CA 91125

11 *Corresponding author: dcrees@caltech.edu

12

13

14 **Abstract**

15 The ATP Binding Cassette (ABC) transporter of mitochondria (*Atm*) from *Arabidopsis thaliana*
16 (*AtAtm3*) has been implicated in the maturation of cytosolic iron-sulfur proteins and heavy metal
17 detoxification, plausibly by exporting glutathione derivatives. Using single-particle cryo-electron
18 microscopy, we have determined structures of *AtAtm3* in multiple conformational states. These
19 structures not only provide a structural framework for defining the alternating access transport
20 cycle, but also highlight an unappreciated feature of the glutathione binding site, namely the
21 paucity of cysteine residues that could potentially form inhibitory mixed disulfides with
22 glutathione. Despite extensive efforts, we were unable to prepare the ternary complex of *AtAtm3*
23 with bound GSSG and MgATP. A survey of structurally characterized type IV ABC transporters
24 that includes *AtAtm3* establishes that while nucleotides are found associated with all
25 conformational states, they are effectively required to stabilize occluded and outward-facing
26 conformations. In contrast, transport substrates have only been observed associated with
27 inward-facing conformations. The absence of structures containing both nucleotide and transport
28 substrate suggests that this ternary complex exists only transiently during the transport cycle.

29

30 **Background**

31 The ATP Binding Cassette (ABC) transporter of mitochondria (Atm) family plays a vital
32 (Leighton and Schatz, 1995), but enigmatic, role broadly related to transition metal homeostasis
33 in eukaryotes (Lill et al., 2014). The best characterized member is *Saccharomyces cerevisiae*
34 *Atm1* (*ScAtm1*) present in the inner membrane of mitochondria (Leighton and Schatz, 1995) and
35 required for formation of cytosolic iron-sulfur cluster containing proteins (Kispal et al., 1999).
36 Defects in *ScAtm1* lead to an overaccumulation of iron in the mitochondria (Kispal et al., 1997).
37 *Atm1* is proposed to transport a sulfur containing intermediate (Kispal et al., 1999) that may also
38 include iron (Pandey et al., 2019). It is also likely to transport a similar sulfur containing species
39 from the mitochondria that is required for the cytoplasmic thiolation of tRNA (Pandey et al., 2018).
40 While the precise substrate that is transported remains unknown, derivatives of glutathione have
41 been implicated based on their ability to stimulate the ATPase activity of *Atm1* (Kuhnke et al.,
42 2006).

43 Structures for *Atm* family members are currently available for *ScAtm1* (Srinivasan et al.,
44 2014), the bacterial homolog *NaAtm1* from *Novosphingobium aromaticivorans* (Lee et al., 2014)
45 and human ABCB6 (Wang et al., 2020); the pairwise sequence identities between these
46 homologous transporters range from 40% to 46%. These proteins occur as homodimers of half-
47 transporters, where each half-transporter contains a transmembrane domain (TMD) followed by
48 the canonical nucleotide binding domain (NBD) that defines the ABC transporter family. Each
49 TMD consists of six transmembrane helices (TMs) that exhibit the exporter type I fold first
50 observed for Sav1866 (Dawson and Locher, 2006); a recent re-classification now identifies this
51 group as type IV ABC transporters (Thomas et al., 2020). The translocation of substrates across
52 the membrane proceeds through an alternating access mechanism involving the ATP dependent
53 interconversion between inward- and outward-facing conformational states. Among the *Atm1*
54 family, these conformations have been most extensively characterized for *NaAtm1* and include

55 the occluded and closed states that provide a structural framework for the unidirectional
56 transport cycle (Fan et al., 2020). Structures of *ScAtm1* with reduced glutathione (GSH)
57 (Srinivasan et al., 2014), and of *NaAtm1* bound to reduced (GSH), oxidized (GSSG) and
58 metallated (GS-Hg-SG) (Lee et al., 2014), have defined the general substrate binding site in the
59 TMD for the transport substrates.

60 Plants have been found to have large numbers of transporters (Hwang et al., 2016),
61 including *Arabidopsis* with three *Atm* orthologues, *AtAtm1*, *AtAtm2*, and *AtAtm3* (Chen et al.,
62 2007). Of these, *AtAtm3* (also known as ABCB25) rescues the *ScAtm1* phenotype (Chen et al.,
63 2007), and has been shown to be associated with maturation of cytosolic iron-sulfur proteins
64 (Kushnir et al., 2001), confer resistance to heavy metals such as cadmium and lead (Kim et al.,
65 2006), and participate in the formation of molybdenum-cofactor containing enzymes (Bernard et
66 al., 2009; Teschner et al., 2010). Unlike yeast, defects in *AtAtm3* are not associated with iron
67 accumulation in mitochondria (Bernard et al., 2009). While the physiological substrate is
68 unknown, *AtAtm3* has been shown to transport oxidized glutathione and glutathione polysulfide
69 (GSSSG), with the persulfidated species perhaps relevant to cytosolic iron-sulfur cluster
70 assembly (Schaedler et al., 2014). The ability of *AtAtm3* to export oxidized glutathione has been
71 implicated in helping stabilize against excessive glutathione oxidation in the mitochondria and
72 thereby serving to maintain a suitable reduction potential (Marty et al., 2019).

73 To help address the functional role(s) of *Atm* transporters, we have determined structures
74 of *AtAtm3* in multiple conformational states by single-particle cryo-electron microscopy (cryoEM).
75 These structures not only provide a structural framework for defining the alternating access
76 transport cycle, but also highlight an unappreciated feature of the glutathione binding site,
77 namely the paucity of cysteine residues that could potentially form inhibitory mixed disulfides
78 during the transport cycle. A survey of structurally characterized members of the type IV family
79 of ABC transporters, including the *Atm1* family, establishes that nucleotides are effectively

80 required for the stabilization of the closed, occluded, and outward-facing conformations. In
81 contrast to the nucleotide states, transport substrates and related inhibitors have only been
82 observed associated with inward-facing conformational states. The absence of structures
83 containing both nucleotide and transport substrate suggests that this ternary complex exists only
84 transiently during the transport cycle.

85

86 **Results**

87 *AtAtm3* contains an N-terminal mitochondrial targeting sequence that directs the
88 translated protein to the mitochondria, where it is cleaved following delivery to the inner
89 membrane. Since this targeting sequence consists of ~80 residues and is anticipated to be
90 poorly ordered, we generated three different N-terminal truncation mutants of *AtAtm3* through
91 deletion of 60, 70 or 80 residues to identify the best-behaved construct. Together with the wild
92 type construct, these three variants were heterologously overexpressed in *E. coli*. The construct
93 with the 80 amino acids deletion showed the highest expression level and proportionally less
94 aggregation by size exclusion chromatography (Figure S1) and hence was used for further
95 functional and structural studies.

96

97 *ATPase activities*

98 Using the 80-residue truncation construct, *AtAtm3* was purified in the detergent dodecyl-
99 β -D-maltoside (DDM) and reconstituted into nanodiscs formed from the membrane scaffolding
100 protein (MSP) 1D1 and the lipid 1-palmitoyl-2-oleoyl-glycero-3-phosphocholine (POPC). The
101 ATPase activity of this construct was measured as a function of MgATP concentration in the
102 absence and presence of either 2.5 mM GSSG or 10 mM GSH, which approximate their
103 physiological concentrations in *E. coli* (Bennett et al., 2009). The rate of ATP hydrolysis was
104 determined by measuring phosphate release using a molybdate based colorimetric ATPase

105 activity assay (Chifflet, 1988). The basal ATPase activity, measured in the absence of
106 glutathione derivatives, was significantly higher in detergent than in nanodiscs (104 versus 7.7
107 nmol min⁻¹ mg⁻¹, respectively; Figures 1ab), while the apparent K_ms for MgATP were within a
108 factor of two (~0.16 mM and 0.08 mM, respectively). The ATPase activity of *AtAtm3* is stimulated
109 by both 2.5 mM GSSG and 10 mM GSH, but the extent of stimulation depends strongly on the
110 solubilization conditions. In nanodiscs, the ATPase rates increase to 32 and 39 nmol min⁻¹ mg⁻¹
111 with 2.5 mM GSSG and 10 mM GSH, respectively, for an overall increase of 4-5x above the
112 basal rate. The ATPase rates for *AtAtm3* in DDM also increase with GSSG and GSH, to 117
113 and 154 nmol min⁻¹ mg⁻¹, respectively. Because of the higher basal ATPase rate in detergent,
114 however, the stimulation effect is significantly less pronounced, corresponding to only a ~50%
115 increase for GSSG stimulation. Little change is observed for the K_ms of MgATP between the
116 presence and absence of glutathione derivatives for either detergent solubilized or nanodisc
117 reconstituted *AtAtm3* (Figure 1).

118

119 *Inward-facing, nucleotide-free conformational states*

120 To map out the transport cycle, we attempted to capture *AtAtm3* in distinct liganded
121 conformational states using single-particle cryoEM. We first determined the structure of *AtAtm3*
122 reconstituted in nanodiscs at 3.4 Å resolution in the absence of either nucleotide or transport
123 substrate (Figure 2a, S2). This structure revealed an inward-facing conformation for *AtAtm3*
124 similar to those observed for the inward-facing conformations for *ScAtm1* (PDB ID: 4myc) and
125 *NaAtm1* (PDB ID: 6vqu) with overall alignment rmsds for the dimer of 2.6 Å (Figure S3a) and 2.1
126 Å (Figure S3b), respectively, and half-transporter alignment rmsds of 2.3 Å and 2.0 Å (Figure
127 S3c), respectively. The primary distinction between these structures is the presence of a ~20
128 amino acid loop between TM1 and TM2 of *AtAtm3* that would be positioned in the intermembrane
129 space and is absent from the structures of *ScAtm1* and *NaAtm1* (Figure 2a, S2de).

130 To further look at the substrate binding, we determined a 3.6 Å resolution single-particle
131 cryoEM structure of *AtAtm3* purified in DDM with bound GSSG (Figure 2b, S4). Although the
132 overall resolution of the reconstruction was moderate (Figure S4d), we were able to model the
133 GSSG molecule into the density map. In this structure, *AtAtm3* adopts an inward-facing
134 conformation, with an overall alignment rmsd of 2.9 Å (Figure S5a) and half-transporter
135 alignment rmsd of 1.6 Å (Figure S5b) comparing to the ligand-free inward-facing structure. The
136 main difference between the two structures is the extent of NBD dimer separation (Figure S5a),
137 where the GSSG bound structure presents a more closed NBD dimer relative to the substrate-
138 free structure. As previously noted with *NaAtm1* (Fan et al., 2020), the TM6 helices in these
139 inward-facing structures of *AtAtm3* adopt a kinked conformation including residues 429-438
140 (Figure 2cd). This opens the backbone hydrogen bonding interactions to create the binding site
141 for GSSG (Figure 2e) with binding pocket residues identified by PDBePISA (Krissinel and
142 Henrick, 2007). The binding mode of GSSG in this *AtAtm3* inward-facing conformation is similar
143 to that observed in the inward-facing structure of the GSSG bound *NaAtm1* (Lee et al., 2014).

144 145 *MgADP-VO₄ stabilized closed and outward-facing conformation*

146 *MgADP-VO₄* has been found to be a potent inhibitor of multiple ATPases through
147 formation of a stable species resembling an intermediate state during ATP hydrolysis (Crans et
148 al., 2004; Davies and Hol, 2004). We determined two structures of *AtAtm3* stabilized with
149 *MgADP-VO₄*, one in the closed conformation with *AtAtm3* reconstituted in nanodiscs at 3.9 Å
150 resolution (Figure 2f, S6), and the other in the outward-facing conformation with *AtAtm3* in DDM
151 at 3.8 Å resolution (Figure 2g, S7). These two structures share an overall alignment rmsd of 1.7
152 Å with the primary difference being a change in separation of the TM helices surrounding the
153 translocation pathway on the side of the transporter facing the intermembrane space (Figure S8).
154 As a result of these changes in the TMDs, access to the intermembrane space is either blocked

155 in the closed conformation (Figure 2f) or is open in the outward-facing conformation (Figure 2g).
156 The changes in the TMDs are reflected in the conformations of TM6, which in the closed
157 structure presents a kinked conformation (Figure 2h), in contrast to the straight conformation in
158 the outward-facing structure that has the backbone hydrogen bonding interaction restored in the
159 helices (Figure 2i). Further, the loops between TM1 and TM2 that are characteristic of the
160 *AtAtm3* transporter are more ordered in the closed conformation than in the outward-facing
161 conformation (Figure 2fg, S5-6). In contrast to the variation in the TMDs, the dimerized NBDs
162 are virtually identical in these two structures with an overall alignment rmsd of 0.8 Å (Figure 2fg,
163 S8).

164

165 Discussion

166 The plant mitochondrial *Atm3* transporter has been implicated in a diverse set of functions
167 associated with transition metal homeostasis that are reflective of the roles that have been
168 described for the broader *Atm1* transporter family. To provide a general framework for
169 addressing the detailed function of this transporter in plants, we have structurally and functionally
170 characterized *Atm3* from *Arabidopsis thaliana*. We first identified a construct of *AtAtm3* with the
171 mitochondrial targeting sequence deleted that expressed well in *E. coli* (Figure S1). Following
172 purification, the ATPase activities of *AtAtm3* were measured in both detergent and MSP
173 nanodiscs as a function of MgATP concentrations (Figure 1). Overall, the ATPase rate measured
174 in detergent is about 5-fold greater than that measured in nanodiscs, perhaps indicative of a
175 more tightly coupled ATPase activity in a membrane-like environment. Both GSH and GSSG
176 stimulate the ATPase activity by increasing V_{max} , with little change observed in the K_m for MgATP.

177 ABC transporters are typically envisioned as utilizing an ‘alternating access’ mechanism, in
178 which the substrate-binding site transitions between inward- and outward- facing conformations
179 coupled to the binding and hydrolysis of ATP. In an idealized two-state model, ABC transporters

180 only adopt these two limiting conformations, but structural characterizations of ABC transporters
181 in the presence of nucleotides and substrate analogs have identified a variety of intermediates,
182 including occluded (with a ligand binding cavity exhibiting little or no access to either side of the
183 membrane) and closed (no ligand binding cavity) conformations. The most extensive analysis of
184 the conformational states of an Atm1 type exporter has been detailed for *NaAtm1* and assigned
185 to various states in the transport cycle (Fan et al., 2020; Lee et al., 2014). In the present work,
186 we have determined four structures of *AtAtm3* in three different conformational states by single
187 particle cryo-EM: two inward-facing conformations (with and without bound GSSG) (Figure 2ab),
188 together with closed and outward-facing states stabilized by MgADP-VO₄ (Figure 2fg). The
189 parallels between the structurally characterized conformations of *AtAtm3* and *NaAtm1* support
190 the idea that these conformational states are relevant to the transport cycle, and not simply an
191 artifact of the specific conditions used to prepare each sample. The conformations observed for
192 *AtAtm3* and *NaAtm1* do not completely correspond, however; most notably, the outward-facing
193 conformation observed for *AtAtm3* had not been previously observed with *NaAtm1* (Fan et al.,
194 2020; Lee et al., 2014), while the occluded conformations found with *NaAtm1* were not observed
195 for *AtAtm3*. The major differences between the closed and outward-facing conformations of
196 *AtAtm3* stabilized with MgADP-VO₄ are in the arrangements of the TMDs, while the NBDs are
197 closely superimposable. In contrast, the primary differences between the two structures of
198 inward-facing conformations of *AtAtm3* are in the relative positioning of the NBDs which are
199 more widely separated in the apo structure relative to the GSSG bound structure; the
200 arrangements of the TMDs in the dimer are similar in both structures.

201 The conformational changes in the TMDs underlying the transport cycle are associated with
202 changes in the extent of kinking of TM6 and the positioning of TM4-TM5 relative to the core
203 formed by the remaining four TM helices. As noted for *NaAtm1*, we observed kinked TM6s in
204 the inward-facing and closed state of *AtAtm3* (Figure 2cdh), but not the outward-facing

205 conformation (Figure 2i). These conformational changes lead to changes in the volume of the
206 central cavity forming the glutathione binding site. Using the program CastP (Tian et al., 2018)
207 with a probe radius of 2.5 Å, the cavity volumes of the inward-facing apo and GSSG bound
208 structures were measured to be ~6,500 Å³ (Figure 3a) and ~4,300 Å³ (Figure 3b), respectively,
209 while the closed conformation exhibits a cavity volume of ~300 Å³ (Figure 3c), and the outward-
210 facing conformation has a cavity volume of ~5,700 Å³ (Figure 3d). We also measured the
211 accessible solvent areas (ASA) of the key residues forming the binding site for GSSG in the
212 different conformational states using Areaimol in CCP4 (Winn et al., 2011); the ASA of the
213 inward-facing, inward-facing with GSSG bound, closed and outward-facing structures are
214 ~1,500 Å², ~1,100 Å², ~900 Å², and ~1,300 Å², which are also highly correlated with the cavity
215 volume calculations. Most of the binding pocket residues remain exposed in all conformations
216 with a few having large relative changes than others (Figure S9). Further, the cavity volume
217 measurements are comparable to those calculated for *NaAtm1* (Fan et al., 2020). The
218 similarities in conformational states between *NaAtm1* and *AtAtm3* indicate these transporters
219 follow the same basic mechanism, in which straightening of TM6s in the transition from inward-
220 to outward-conformation leads to the release of substrate to the opposite side of the membrane.
221 Following substrate release, the transporter resets to the inward-facing conformation through
222 the closed conformation adopted after ATP hydrolysis; the decreased size of the substrate
223 binding cavity helps enforce substrate release and unidirectionality of substrate transport.

224 The binding pocket for GSSG identified in this work primarily consists of residues from
225 TM5 and TM6, with additional contributions from residues in TM3 and TM4. The GSSG binding
226 site for *AtAtm3* largely overlaps with that identified previously for *NaAtm1* (Lee et al., 2014) and
227 for the binding of reduced GSH to *ScAtm1* (Srinivasan et al., 2014). Inspection of a sequence
228 alignment of *Atm1* homologs (Figure S10) reveals that those residues forming the glutathione
229 binding site are largely conserved, particularly if they are involved in polar interactions. A striking

230 feature is the stretch of residues from P432 to R441 in the middle of TM6 (*AtAtm3* sequence
231 numbering) with sequence PLNFLGSVYR with a high degree of sequence conservation. P432
232 is associated with the TM6 kink in inward-facing conformations that permits formation of
233 hydrogen bonds between exposed peptide groups with GSSG (Lee et al., 2014); as TM6
234 straightens in the occluded and outward-facing conformations, these peptide groups are no
235 longer available to bind the transport substrate (Fan et al., 2020). A sequence alignment of the
236 structurally characterized *AtAtm3*, *NaAtm1*, *ScAtm1* and human ABCB7 and ABCB6 (Figure S2)
237 transporters establishes that residues in the binding pockets are conserved, including T317,
238 R324, R328, N387, Q390, L433, G437 and R441 (Figure S10). The conservation of binding
239 pocket residues as calculated by the program ConSurf (Landau et al., 2005) is illustrated in
240 Figure 4 suggests that the substrates for these transporters may share common features, such
241 as the glutathione backbone. Positions such where sequence variability is evident, such as
242 residue 435 (Figure 4B and S9), may reflect the binding of distinct GSSG-derivatives by different
243 eukaryotic and prokaryotic homologs.

244 An important property of disulfide containing compounds such as oxidized glutathione is
245 that they can undergo disulfide – thiol exchange with free -SH groups (Creighton, 1984; Nagy,
246 2013). This reactivity creates potential challenges for proteins such as *AtAtm3* since reaction of
247 a disulfide containing ligand such as GSSG with the thiol-containing side chain of cysteine could
248 lead to formation of the mixed disulfide, thereby covalently connecting glutathione to the protein
249 and releasing reduced GSH. Formation of the covalently linked mixed disulfide would be
250 expected to restrict the access of exogenous ligands to the substrate binding cavity and hence
251 would inhibit transport. For membrane proteins, cysteine residues are present in transmembrane
252 helices with a frequency of about 1% (Baeza-Delgado et al., 2013). Although no cysteines
253 residues are present in the *AtAtm3* binding pocket, we analyzed additional *Atm3* homologs from
254 plants. For this analysis, we used the NCBI blastp server (Altschul et al., 1997) and selected 410

255 sequences with a sequence identity of 50% to 100% and query coverage of 80% to 100% with
256 *AtAtm3*, Within the six TM helices, the overall presence of cysteines was found to be ~0.4%. In
257 this alignment, no cysteines were found in residues forming the glutathione binding cavity (Figure
258 5); more strikingly, no cysteine residues were found at any position of TM6 for these homologs
259 (Figure 5f). Cysteines that are present in the TMs are either distant from the binding site, such
260 as position 405 in TM5 of *AtAtm3* (Figure 5eg) or if they are closer to the binding site, are
261 positioned on the opposite side of the TMs, such as positions 149, 215, 290 and 307 (Figure
262 5abcd). The lack of cysteines (Figure 5g) may reflect a design feature in the glutathione binding
263 site, namely cysteines that could potentially form inhibitory mixed disulfides during the transport
264 cycle are excluded from *Atm3*.

265 As a general strategy to stabilize ABC transporters in distinct conformational states,
266 different nucleotides or transport substrates are mixed with the transporter. The expectation is
267 that a particular set of ligands will stabilize a specific conformational state, and so we were
268 surprised to have captured with MgADP-VO₄ both a closed conformation in MSP nanodiscs and
269 an outward-facing conformation in detergent. Given the similarities in the NBDs between these
270 two structures, the distinctive arrangements of the TMDs between the closed and outward-facing
271 conformations presumably arises from differences in the TMD environment provided by MSP
272 nanodiscs and DDM, respectively. Furthermore, this phenomenon of obtaining different
273 conformational states with MgADP-VO₄ is not unprecedented, however, since previously
274 determined structures of MgADP-VO₄ stabilized ABC exporters include *NaAtm1* in the closed
275 conformation (Fan et al., 2020), *Thermus thermophilus* TmrAB in the occluded and outward-
276 facing conformations (Hofmann et al., 2019) and *Escherichia coli* MsbA in the closed
277 conformation (Mi et al., 2017).

278 Despite extensive efforts, we were unable to prepare the ternary complex of *AtAmt3* with
279 bound GSSG and MgATP. To assess more generally the relationship between the

280 conformational states of ABC exporters and the presence or absence of nucleotide and transport
281 substrate, we systematically compared the conformations of 80 half-transporters from the
282 available structures of type IV ABC transporters (Table S2). To define the conformational state
283 in a consistent fashion, we performed a principal component analysis (PCA) of these half-
284 transporter structures (see Material and Methods); the principal component is dominated by the
285 conformational state of the TMDs, which represents ~62% of total conformational change from
286 the inward-facing to the outward-facing conformation. The distribution of component 1 of the
287 PCA is shown in Figure 6 with the most extreme inward-facing conformations to the left and the
288 outward-facing conformations to the right.

289 To validate this approach, we color coded each structure according to their published
290 conformational state (Figure 6a). It is evident that outward-facing conformations occur on the
291 right-handed side of the figure with component 1 values between -25 and 0 Å², while occluded,
292 closed and inward-facing conformations cluster around -25, -25 and -100 Å², respectively. Hence,
293 the magnitude of the principal component does capture the expected trends in conformational
294 state, with increasing values corresponding to a progression from inward-facing to outward-
295 facing conformations. The correspondence is not exact, however, since assigned conformational
296 states overlap, which could reflect either limitations of the principal component analysis, and/or
297 inconsistent assignments of conformational states between different structures. We further note
298 that some conformational states have a very wide distribution, particularly the inward-facing
299 conformations, with several structures exhibiting widely separated subunits (with values for
300 component 1 below -150 Å²). Using the principal component analysis, we could relate protein
301 conformation to binding of nucleotides (Figure 6b) and substrates/inhibitors (Figure 6c). This
302 analysis establishes that occluded and outward-facing conformations are largely nucleotide
303 bound with either ATP or an ATP analog, but there are exceptions, most notably the original
304 ADP bound structure of Sav1866 ((Dawson and Locher, 2006); a similar Sav1866 structure was

305 subsequently solved with bound AMPPNP (Dawson and Locher, 2007)). Inward-facing
306 conformations are observed in both nucleotide-free and nucleotide bound forms (Figure 6b).
307 Only the MgADP-VO₄ bound structures are exclusively found to occupy a small conformational
308 space in the closed/outward-facing region. In contrast to the binding of nucleotides to all
309 conformational states of these transporters, a distinct pattern is observed for the binding of
310 transport substrates where the transporter invariably adopts the inward-facing conformation
311 (Figure 6c). Intriguingly, no structures to date have been published that contain both nucleotide
312 and transport substrate, suggesting that this ternary complex exists only transiently during the
313 transport cycle. As this is a key intermediate for understanding how the binding of transport
314 substrate stimulates the ATPase activity, characterization of the ternary complex represents an
315 outstanding gap in the mechanistic characterization of ABC exporters.

316

317 **Material and Methods**

318 *Cloning, expression and purification*

319 A pET-21a (+) plasmid containing the full-length *Arabidopsis thaliana* Atm3 (*AtAtm3*)
320 gene with a C-terminal 6x-His tag was purchased from Genscript (Genscript, NJ). Mutagenesis
321 reactions generating the N-terminal 60, 70 and 80 amino acids deletion mutants were carried
322 out with the Q5 mutagenesis kit (New England Biolabs, MA). All *AtAtm3* constructs were
323 overexpressed in *Escherichia coli* BL21-gold (DE3) cells (Agilent Technologies, CA) using ZYM-
324 5052 autoinduction media as described previously (Fan et al., 2020). Cells were harvested by
325 centrifugation and stored at -80 °C.

326 For purification, frozen cell pellets were resuspended in lysis buffer containing 100 mM
327 NaCl, 20 mM Tris, pH 7.5, 40 mM imidazole, pH 7.5, 10 mM MgCl₂ and 5 mM β-mercaptoethanol
328 (BME) in the presence of lysozyme, DNase, and cOmplete protease inhibitor tablet (Roche,
329 Basel, Switzerland). The resuspended cells were lysed with an M-110L pneumatic microfluidizer

330 (Microfluidics, MA). Unlysed cells and cell debris were removed by centrifugation at ~20,000 x g
331 for 30 minutes at 4 °C. The membrane fraction containing *AtAtm3* was collected by
332 ultracentrifugation at ~113,000 x g for an hour at 4 °C. The membrane fraction was then
333 resuspended in buffer containing 100 mM NaCl, 20 mM Tris, pH 7.5, 40 mM imidazole, pH 7.5,
334 and 5 mM BME and further solubilized by stirring with the addition of 1% n-dodecyl- β -D-
335 maltopyranoside (DDM) (Anatrace, OH) for an hour at 4 °C. The DDM solubilized membrane
336 was ultracentrifuged at ~113,000 x g for 45 minutes at 4 °C to remove any unsolubilized material.
337 The supernatant was loaded onto a prewashed NiNTA column. NiNTA wash buffer contained
338 100 mM NaCl, 20 mM Tris, pH 7.5, 50 mM imidazole, pH 7.5, 5 mM BME and 0.02% DDM, while
339 the elution buffer contained the same components, but with 380 mM imidazole. The eluent was
340 subjected to size exclusion chromatography using HiLoad 16/60 Superdex 200 (GE Healthcare,
341 IL) with buffer containing 100 mM NaCl, 20 mM Tris, pH 7.5, 5 mM BME and 0.02% DDM. Peak
342 fractions were collected and concentrated to ~10 mg/ml using Amicon concentrators (Millipore,
343 MA).

344

345 *ATPase activity assay*

346 ATPase assays were carried out as described previously for both the detergent purified
347 and the reconstituted nanodisc samples (Fan et al., 2020) using a molybdate based colorimetric
348 assay (Chifflet, 1988).

349

350 *Nanodisc reconstitution*

351 For the *AtAtm3* structures in nanodiscs, the reconstitution was performed following the
352 previously described protocol (Fan et al., 2020). The reconstitution was done with a 1:4:130
353 molar ratio of *AtAtm3*: membrane scaffolding protein (MSP) 1D1: 1-palmitoyl-2-oleoyl-glycero-
354 3-phosphocholine (POPC) (Avanti Polar Lipids, AL). After overnight incubation at 4 °C, the

355 samples were subjected to size exclusion chromatography with a Superdex 200 Increase 10/300
356 column (GE Healthcare, IL). The peak fractions were directly used for grid preparation with the
357 reconstituted samples at ~0.5 mg/ml. For the structure of *AtAtm3* with GSSG bound in the
358 inward-facing conformation, the detergent purified protein was incubated with 10 mM GSSG, pH
359 7.5 at 4 °C for an hour with *AtAtm3* at 4 mg/ml before freezing grids.

360

361 *Grid preparation*

362 For the *AtAtm3* structure with MgADP-VO₄ bound in the outward-facing conformation, the
363 detergent purified protein was incubated with 4 mM ATP, pH 7.5, 4 mM MgCl₂ and 4 mM VO₄³⁻
364 with protein at 5 mg/ml at 4 °C overnight before freezing grids. For all grids, 3 μL of protein
365 solution was applied to freshly glow-discharged UltrAuFoil 2/2 200 mesh grids (apo inward-
366 facing conformation and closed conformation, both in nanodiscs) and UltrAuFoil 1.2/1.3 300
367 mesh grids (Electron Microscopy Sciences, PA) (GSSG bound inward-facing conformation and
368 outward-facing conformation, both in detergent) and blotted for 4 to 5 seconds with a blot force
369 of 0 and 100% humidity at room temperature using the VitroBot Mark IV (Thermo-Fisher, MA).

370

371 *Single-particle cryoEM data collection, processing and refinement*

372 Datasets for the inward-facing conformations in apo and GSSG bound states, and the
373 outward-facing conformation with MgADP-VO₄ bound were collected with a Gatan K3 direct
374 electron detector (Gatan, CA) on a 300 keV Titan Krios (Thermo-Fisher, MA) in the super-
375 resolution mode using SerialEM at the Caltech CryoEM facility. These datasets were collected
376 using a defocus range between -1.5 to -3.0 μm and a total dosage of 60 e⁻/Å². The dataset for
377 the closed conformation with MgADP-VO₄ bound was collected with a Falcon 4 direction electron
378 detector (Thermo-Fisher, MA) on a 300 keV Titan Krios (Thermo-Fisher, MA) in the super-

379 resolution mode using EPU (Thermo-Fisher, MA) at the Stanford-SLAC Cryo-EM Center (S2C2)
380 with a defocus range between -1.5 and -2.1 μm and a total dosage of $\sim 48 \text{ e}^-/\text{\AA}^2$.

381 Detailed processing workflows of all single-particle cryoEM datasets are included in
382 Figure S2, S4, S6 and S7. Datasets for the inward-facing conformation in apo and GSSG bound
383 states, and the outward-facing conformation with MgADP-VO₄ bound were motion corrected with
384 the patch motion correction in cryoSPARC 2 (Punjani et al., 2017), while the dataset for the
385 closed conformation with MgADP-VO₄ bound was motion corrected with motioncor2 (Zheng et
386 al., 2017). The subsequent processing of all datasets was performed in a similar fashion. The
387 contrast transfer function (CTF) parameters were estimated with patch CTF estimation in
388 cryoSPARC 2 (Punjani et al., 2017). Particles were picked with blob picker using a particle
389 diameter of 80 to 160 \AA and then extracted. Rounds of two-dimensional (2D) and three-
390 dimensional (3D) classifications were performed, leaving 157,762, 259,020, 140,569 and
391 103,161 particles for the inward-facing apo, inward-facing GSSG bound, closed, and outward-
392 facing conformations, respectively. The final reconstructions were refined with homogeneous,
393 non-uniform and local refinements in cryoSPARC 2 with C2 symmetry (Punjani et al., 2017). The
394 masks used in local refinements were generated in Chimera (Pettersen et al., 2004).

395 The initial model of the *AtAtm3* inward-facing conformation in apo state was obtained
396 using the inward-facing occluded structure of *NaAtm1* (PDB ID: 6pam) as a starting model (Fan
397 et al., 2020). The model fitting was carried out with phenix.dock_in_map (Liebschner et al., 2019).
398 That apo inward-facing conformation model of *AtAtm3* was subsequently used as the starting
399 model for the inward-facing GSSG bound structure. The previous *NaAtm1* closed conformation
400 structure (PDB: 6par) was used as the starting model for both the closed and the outward-facing
401 conformations. Model building and ligand fitting were carried out manually in Coot (Emsley et al.,
402 2010) and the structures were refined with phenix.real_space_refine (Liebschner et al., 2019).

403

404 *Structure superposition*

405 Structure superpositions for calculating the root mean square deviations (rmsds) between
406 different structures were performed with the SSM option in *Coot* (Emsley et al., 2010).

407

408 *Principal component analysis*

409 The objective of our principal component analysis (PCA) was to provide a quantitative
410 foundation for relating the binding of nucleotides and transported ligands to the conformational
411 state of type IV ABC transporters that include *AtAtm3* and related *Atm1* transporters (Thomas
412 et al., 2020). For this purpose, we first identified 10 polypeptide stretches containing 7 to 21
413 residues at equivalent positions in 80 structurally characterized type IV transporters (Table S2),
414 including residues from the TMD and from the NBD. In this sequence selection process, a single
415 half-transporter was used for homodimeric transporters, and both half-transporters were used
416 for heterodimeric transporters, whether encoded by two different half-transporter peptides or on
417 a single peptide. The coordinates of C α positions for the selected residues were extracted and
418 aligned to that of the outward-facing conformation of Sav1866 (PDB ID: 2hyd) based on the C α
419 coordinates in TM3 and TM6, which were previously found to provide a useful reference frame
420 for studying conformational changes (Lee et al., 2014). *AtAtm3* residues used in alignment: 140-
421 160, 225-245, 255-275, 322-342, 362-382, 423-443, 504-513, 517-524, 618-632 and 681-688.
422 *NaAtm1* residues used in alignment: 36-56, 107-127, 137-157, 204-224, 244-264, 305-325, 386-
423 395, 399-406, 500-514 and 563-570.

424 The PCA was performed using the “essential dynamics” algorithm (Amadei et al., 1993).
425 The full transporter was used in these calculations with the outward-facing state of Sav1866
426 (PDB ID: 2hyd) serving as the reference state. The first component captured 62% of the overall
427 conformational variation among these structures, and so the eigenvalues corresponding to this
428 component were used to order the different structures along a single axis (Figure 6). In general,

429 the conformational states assigned to each structure parallel those obtained from the PCA
430 analysis; differences likely reflect the absence of standardized definitions for assigning the
431 conformational states of ABC transporters as well as the limitations of this PCA analysis,
432 particularly the use of only the dominant eigenvector.

433

434 **Funding**

435 D.C.R. is a Howard Hughes Medical Institute Investigator.

436

437 **Author contributions**

438 C.F. and D.C.R. designed the research; C.F. performed the research; C.F. and D.C.R. analyzed
439 the data; and C.F. and D.C.R. prepared the manuscript.

440

441 **Competing Interests**

442 The authors declare no competing interests.

443

444 **Data availability**

445 The atomic coordinates for inward-facing, inward-facing with GSSG bound, closed and outward-
446 facing conformations were separately deposited in the Protein Data Bank (PDB) and the Electron
447 Microscopy Data Bank (EMDB) with accession codes: PDB 7N58, 7N59, 7N5A and 7N5B;
448 EMDB EMD-24182, EMD-24183, EMD-24184 and EMD-24185. The plasmid encoding full-
449 length *AtAtm3* and the *AtAtm3* with N-terminal 80 residue deletion were deposited in Addgene
450 with Addgene ID 172321 and 173045, respectively. The raw data for ATPase assays presented
451 in Figure 1 are provided in Supplementary File 1, while the `essdyn.f` Fortran source code used
452 for the PCA analysis is provided as Source Code 1.

453

454 **Acknowledgments**

455 We thank Andrey Malyutin, Songye Chen and Corey Hecksel for their support during single-
456 particle cryo-EM data collections. Cryo-electron microscopy was performed in the Beckman
457 Institute Resource Center for cryo-Electron Microscopy at Caltech and at the Stanford-SLAC
458 Cryo-EM Center (S2C2). The S2C2 is supported by the National Institutes of Health Common
459 Fund Transformative High Resolution Cryo-Electron Microscopy program. We thank the
460 Beckman Institute for their support of the cryo-EM facility at Caltech.

461

462

463 **References**

- 464 Altschul, S.F., Madden, T.L., Schaffer, A.A., Zhang, J., Zhang, Z., Miller, W., and Lipman, D.J. (1997).
465 Gapped BLAST and PSI-BLAST: a new generation of protein database search programs. *Nucleic Acids*
466 *Research* *25*, 3389-3402.
- 467 Amadei, A., Linssen, A.B., and Berendsen, H.J. (1993). Essential dynamics of proteins. *Proteins* *17*,
468 412-425.
- 469 Baeza-Delgado, C., Marti-Renom, M.A., and Mingarro, I. (2013). Structure-based statistical analysis of
470 transmembrane helices. *European Biophysics Journal* *42*, 199-207.
- 471 Bennett, B.D., Kimball, E.H., Gao, M., Osterhout, R., Van Dien, S.J., and Rabinowitz, J.D. (2009).
472 Absolute metabolite concentrations and implied enzyme active site occupancy in *Escherichia coli*.
473 *Nature Chemical Biology* *5*, 593-599.
- 474 Bernard, D.G., Cheng, Y., Zhao, Y., and Balk, J. (2009). An allelic mutant series of ATM3 reveals its
475 key role in the biogenesis of cytosolic iron-sulfur proteins in *Arabidopsis*. *Plant physiology* *151*, 590-
476 602.
- 477 Chen, S., Sanchez-Fernandez, R., Lyver, E.R., Dancis, A., and Rea, P.A. (2007). Functional
478 characterization of AtATM1, AtATM2, and AtATM3, a subfamily of *Arabidopsis* half-molecule ATP-
479 binding cassette transporters implicated in iron homeostasis. *Journal of Biological Chemistry* *282*,
480 21561-21571.
- 481 Chifflet, S., Torriglia, A., Chiesa, R., and Tolosa, S. (1988). A method for the determination of inorganic
482 phosphate in the presence of labile organic phosphate and high concentration of protein: application to
483 lens ATPases. *Analytical biochemistry* *168*, 1-4.
- 484 Crans, D.C., Smee, J.J., Gaidamauskas, E., and Yang, L. (2004). The chemistry and biochemistry of
485 vanadium and the biological activities exerted by vanadium compounds. *Chemical Reviews* *104*, 849-
486 902.
- 487 Creighton, T.E. (1984). Disulfide bond formation in proteins. *Methods Enzymology* *107*, 305-329.
- 488 Davies, D.R., and Hol, W.G. (2004). The power of vanadate in crystallographic investigations of
489 phosphoryl transfer enzymes. *FEBS Letters* *577*, 315-321.
- 490 Dawson, R.J., and Locher, K.P. (2006). Structure of a bacterial multidrug ABC transporter. *Nature* *443*,
491 180-185.
- 492 Dawson, R.J., and Locher, K.P. (2007). Structure of the multidrug ABC transporter Sav1866 from
493 *Staphylococcus aureus* in complex with AMP-PNP. *FEBS Letters* *581*, 935-938.
- 494 Emsley, P., Lohkamp, B., Scott, W.G., and Cowtan, K. (2010). Features and development of *Coot*. *Acta*
495 *Crystallographica D Biological Crystallography* *66*, 486-501.
- 496 Fan, C., Kaiser, J.T., and Rees, D.C. (2020). A structural framework for unidirectional transport by a
497 bacterial ABC exporter. *Proceedings of the National Academy of Sciences of the United States of*
498 *America* *117*, 19228-19236.

- 499 Hofmann, S., Januliene, D., Mehdipour, A.R., Thomas, C., Stefan, E., Bruchert, S., Kuhn, B.T.,
500 Geertsma, E.R., Hummer, G., Tampe, R., *et al.* (2019). Conformation space of a heterodimeric ABC
501 exporter under turnover conditions. *Nature* *571*, 580-583.
- 502 Hwang, J.U., Song, W.Y., Hong, D., Ko, D., Yamaoka, Y., Jang, S., Yim, S., Lee, E., Khare, D., Kim, K.,
503 *et al.* (2016). Plant ABC transporters enable many unique aspects of a terrestrial plant's lifestyle.
504 *Molecular Plant* *9*, 338-355.
- 505 Kim, D.Y., Bovet, L., Kushnir, S., Noh, E.W., Martinoia, E., and Lee, Y. (2006). AtATM3 is involved in
506 heavy metal resistance in *Arabidopsis*. *Plant physiology* *140*, 922-932.
- 507 Kispal, G., Csere, P., Guiard, B., and Lill, R. (1997). The ABC transporter Atm1p is required for
508 mitochondrial iron homeostasis. *FEBS Letters* *418*, 346-350.
- 509 Kispal, G., Csere, P., Prohl, C., and Lill, R. (1999). The mitochondrial proteins Atm1p and Nfs1p are
510 essential for biogenesis of cytosolic Fe/S proteins. *The EMBO Journal* *18*, 3981-3989.
- 511 Krissinel, E., and Henrick, K. (2007). Inference of macromolecular assemblies from crystalline state. *J*
512 *Mol Biol* *372*, 774-797.
- 513 Kuhnke, G., Neumann, K., Muhlenhoff, U., and Lill, R. (2006). Stimulation of the ATPase activity of the
514 yeast mitochondrial ABC transporter Atm1p by thiol compounds. *Molecular Membrane Biology* *23*, 173-
515 184.
- 516 Kushnir, S., Babiychuk, E., Storozhenko, S., Davey, M.W., Papenbrock, J., De Rycke, R., Engler, G.,
517 Stephan, U.W., Lange, H., Kispal, G., *et al.* (2001). A mutation of the mitochondrial ABC transporter
518 Sta1 leads to dwarfism and chlorosis in the *Arabidopsis* mutant starik. *Plant Cell* *13*, 89-100.
- 519 Landau, M., Mayrose, I., Rosenberg, Y., Glaser, F., Martz, E., Pupko, T., and Ben-Tal, N. (2005).
520 ConSurf 2005: the projection of evolutionary conservation scores of residues on protein structures.
521 *Nucleic Acids Research* *33*, W299-W302.
- 522 Lee, J.Y., Yang, J.G., Zhitnitsky, D., Lewinson, O., and Rees, D.C. (2014). Structural basis for heavy
523 metal detoxification by an Atm1-type ABC exporter. *Science* *343*, 1133-1136.
- 524 Leighton, J., and Schatz, G. (1995). An ABC transporter in the mitochondrial inner membrane is
525 required for the normal growth of yeast. *The EMBO Journal* *14*, 188-195.
- 526 Liebschner, D., Afonine, P.V., Baker, M.L., Bunkoczi, G., Chen, V.B., Croll, T.I., Hintze, B., Hung, L.W.,
527 Jain, S., McCoy, A.J., *et al.* (2019). Macromolecular structure determination using X-rays, neutrons and
528 electrons: recent developments in Phenix. *Acta Crystallographica Section D Structural Biology* *75*, 861-
529 877.
- 530 Lill, R., Srinivasan, V., and Muhlenhoff, U. (2014). The role of mitochondria in cytosolic-nuclear iron-
531 sulfur protein biogenesis and in cellular iron regulation. *Current Opinion in Microbiology* *22*, 111-119.
- 532 Marty, L., Bausewein, D., Muller, C., Bangash, S.A.K., Moseler, A., Schwarzlander, M., Muller-
533 Schussele, S.J., Zechmann, B., Riendet, C., Balk, J., *et al.* (2019). *Arabidopsis* glutathione reductase 2
534 is indispensable in plastids, while mitochondrial glutathione is safeguarded by additional reduction and
535 transport systems. *New Phytologist* *224*, 1569-1584.
- 536 Mi, W., Li, Y., Yoon, S.H., Ernst, R.K., Walz, T., and Liao, M. (2017). Structural basis of MsbA-mediated
537 lipopolysaccharide transport. *Nature* *549*, 233-237.

- 538 Nagy, P. (2013). Kinetics and mechanisms of thiol-disulfide exchange covering direct substitution and
539 thiol oxidation-mediated pathways. *Antioxidants & Redox Signaling* *18*, 1623-1641.
- 540 Pandey, A., Pain, J., Dziuba, N., Pandey, A.K., Dancis, A., Lindahl, P.A., and Pain, D. (2018).
541 Mitochondria export sulfur species required for cytosolic tRNA thiolation. *Cell Chemical Biology* *25*,
542 738-748 e733.
- 543 Pandey, A.K., Pain, J., Dancis, A., and Pain, D. (2019). Mitochondria export iron-sulfur and sulfur
544 intermediates to the cytoplasm for iron-sulfur cluster assembly and tRNA thiolation in yeast. *Journal of*
545 *Biological Chemistry* *294*, 9489-9502.
- 546 Pettersen, E.F., Goddard, T.D., Huang, C.C., Couch, G.S., Greenblatt, D.M., Meng, E.C., and Ferrin,
547 T.E. (2004). UCSF Chimera--a visualization system for exploratory research and analysis. *Journal of*
548 *Computational Chemistry* *25*, 1605-1612.
- 549 Punjani, A., Rubinstein, J.L., Fleet, D.J., and Brubaker, M.A. (2017). cryoSPARC: Algorithms for rapid
550 unsupervised cryo-EM structure determination. *Nature Methods* *14*, 290-296.
- 551 Schaedler, T.A., Thornton, J.D., Kruse, I., Schwarzlander, M., Meyer, A.J., van Veen, H.W., and Balk,
552 J. (2014). A conserved mitochondrial ATP-binding cassette transporter exports glutathione polysulfide
553 for cytosolic metal cofactor assembly. *Journal of Biological Chemistry* *289*, 23264-23274.
- 554 Srinivasan, V., Pierik, A.J., and Lill, R. (2014). Crystal structures of nucleotide-free and glutathione-
555 bound mitochondrial ABC transporter Atm1. *Science* *343*, 1137-1140.
- 556 Teschner, J., Lachmann, N., Schulze, J., Geisler, M., Selbach, K., Santamaria-Araujo, J., Balk, J.,
557 Mendel, R.R., and Bittner, F. (2010). A novel role for *Arabidopsis* mitochondrial ABC transporter ATM3
558 in molybdenum cofactor biosynthesis. *Plant Cell* *22*, 468-480.
- 559 Thomas, C., Aller, S.G., Beis, K., Carpenter, E.P., Chang, G., Chen, L., Dassa, E., Dean, M., Duong
560 Van Hoa, F., Ekiert, D., *et al.* (2020). Structural and functional diversity calls for a new classification of
561 ABC transporters. *FEBS Letters*.
- 562 Tian, W., Chen, C., Lei, X., Zhao, J., and Liang, J. (2018). CASTp 3.0: Computed atlas of surface
563 topography of proteins. *Nucleic Acids Research* *46*, W363-W367.
- 564 Wang, C., Cao, C., Wang, N., Wang, X., Wang, X., and Zhang, X.C. (2020). Cryo-electron microscopy
565 structure of human ABCB6 transporter. *Protein Science* *29*, 2363-2374.
- 566 Winn, M.D., Ballard, C.C., Cowtan, K.D., Dodson, E.J., Emsley, P., Evans, P.R., Keegan, R.M.,
567 Krissinel, E.B., Leslie, A.G., McCoy, A., *et al.* (2011). Overview of the CCP4 suite and current
568 developments. *Acta Crystallographica D Biological Crystallography* *67*, 235-242.
- 569 Zheng, S.Q., Palovcak, E., Armache, J.P., Verba, K.A., Cheng, Y., and Agard, D.A. (2017).
570 MotionCor2: anisotropic correction of beam-induced motion for improved cryo-electron microscopy.
571 *Nature Methods* *14*, 331-332.
572

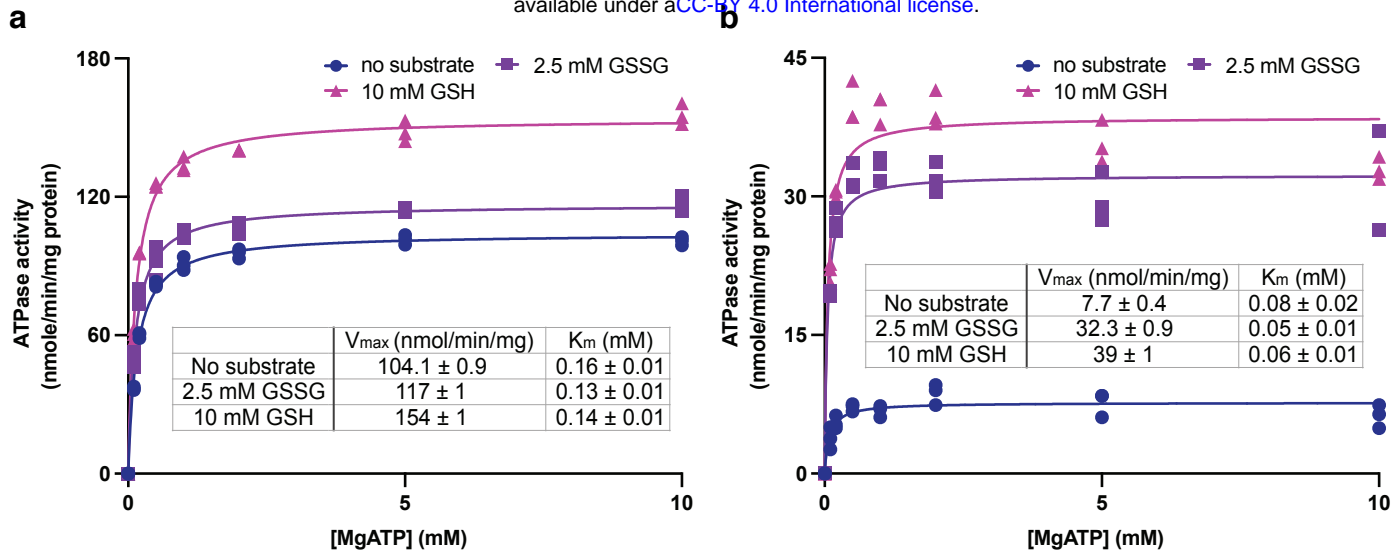


Figure 1. ATPase activities of *AtAtm3*. ATPase activities measured in **a**) the detergent DDM and **b**) nanodiscs formed by membrane scaffolding proteins (MSP) and the lipid 1-palmitoyl-2-oleoyl-glycerol-3-phosphocholine (POPC). The ATPase activities were measured in the absence of substrate (●), at 2.5 mM GSSG (■) and 10 mM GSH (▲). The corresponding values of V_{max} and K_m in different substrate conditions derived from fitting to the Michaelis-Menten equations are indicated. Each condition was measured three times with the individual data points displayed.

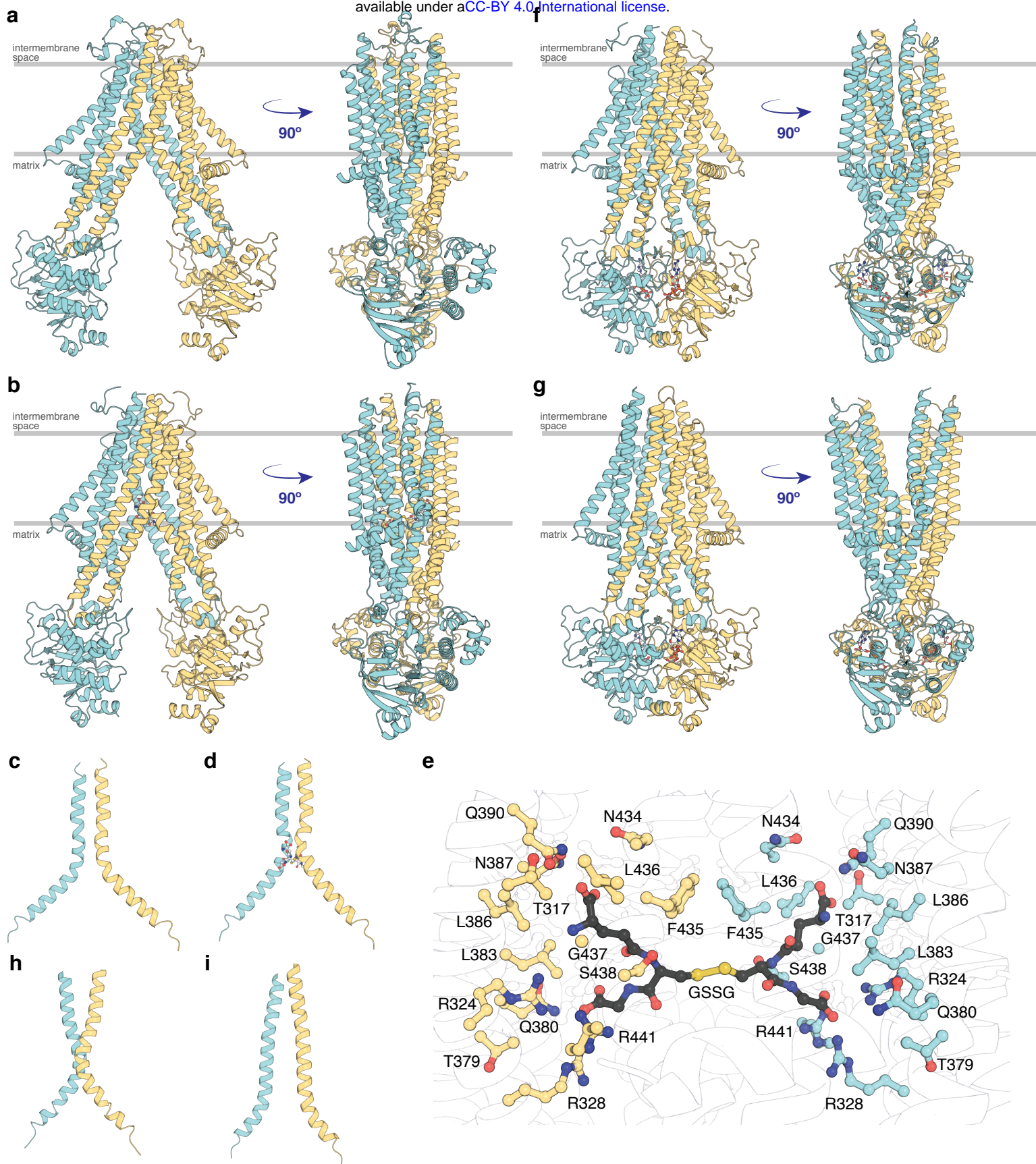


Figure 2. Structures of AtAtm3. **a)** Inward-facing conformation in the apo state. **b)** Inward-facing conformation with GSSG bound. **c)** TM6s (residues 416-460) in the inward-facing conformation. **d)** TM6s in the GSSG-bound inward-facing conformation. The location of GSSG is indicated. **e)** Residues important in stabilizing GSSG binding site, identified by PDBePISA (Krissinel and Henrick, 2007). **f)** Closed conformation with MgADP-VO₄ bound. **g)** Outward-facing conformation with MgADP-VO₄ bound. **h)** TM6s in the closed conformation. **i)** TM6s in the outward-facing conformation.

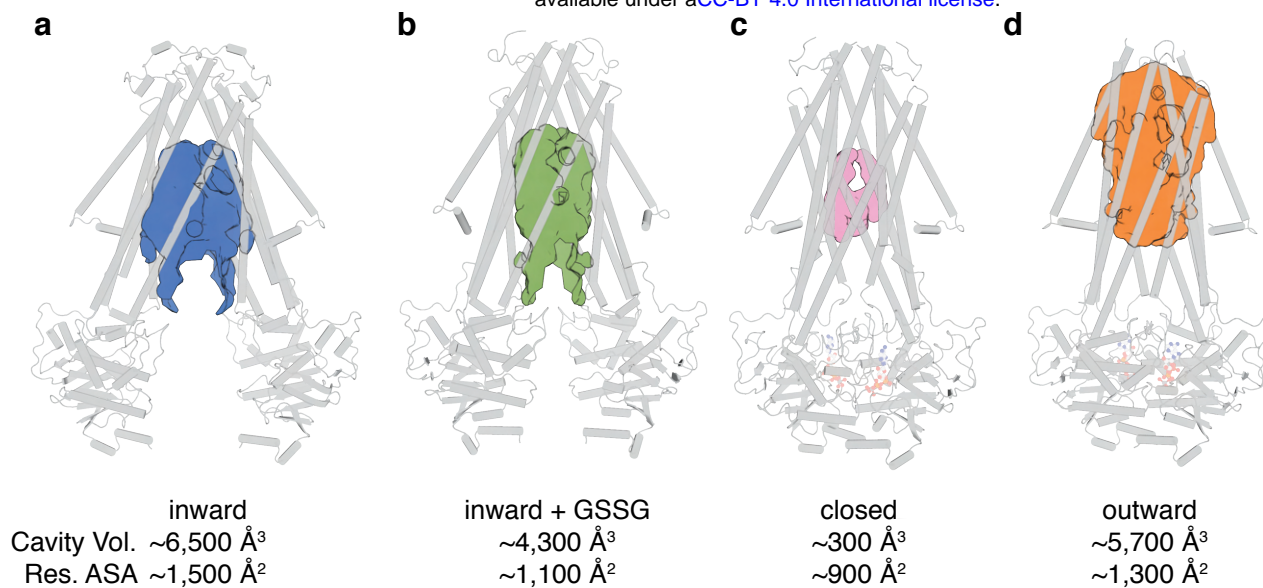


Figure 3. Binding cavity analysis. **a)** Central cavity of the apo inward-facing conformation. **b)** Central cavity of the inward-facing conformation with GSSG bound. **c)** Closed conformation with no central cavity observed. **d)** Central cavity of the outward-facing conformation. Cavity volumes were measured by CastP (Tian et al., 2018) using a probe radius of 2.5 \AA . *AtAtm3* is shown as a grey cartoon representation, while cavities are depicted as color surfaces. The accessible solvent areas (ASA) of the key residues in the GSSG binding pockets of different structures were calculated Areaimol in CCP4 (Winn et al., 2011).

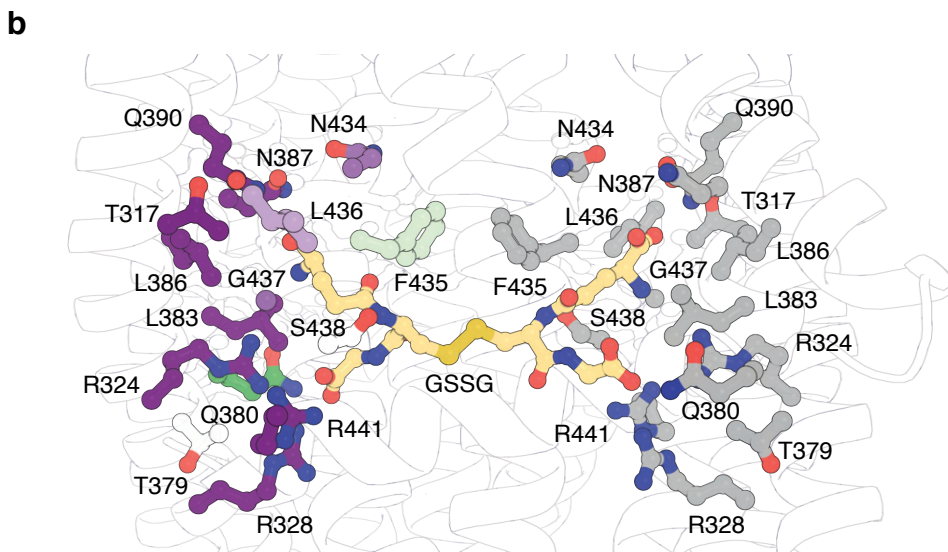
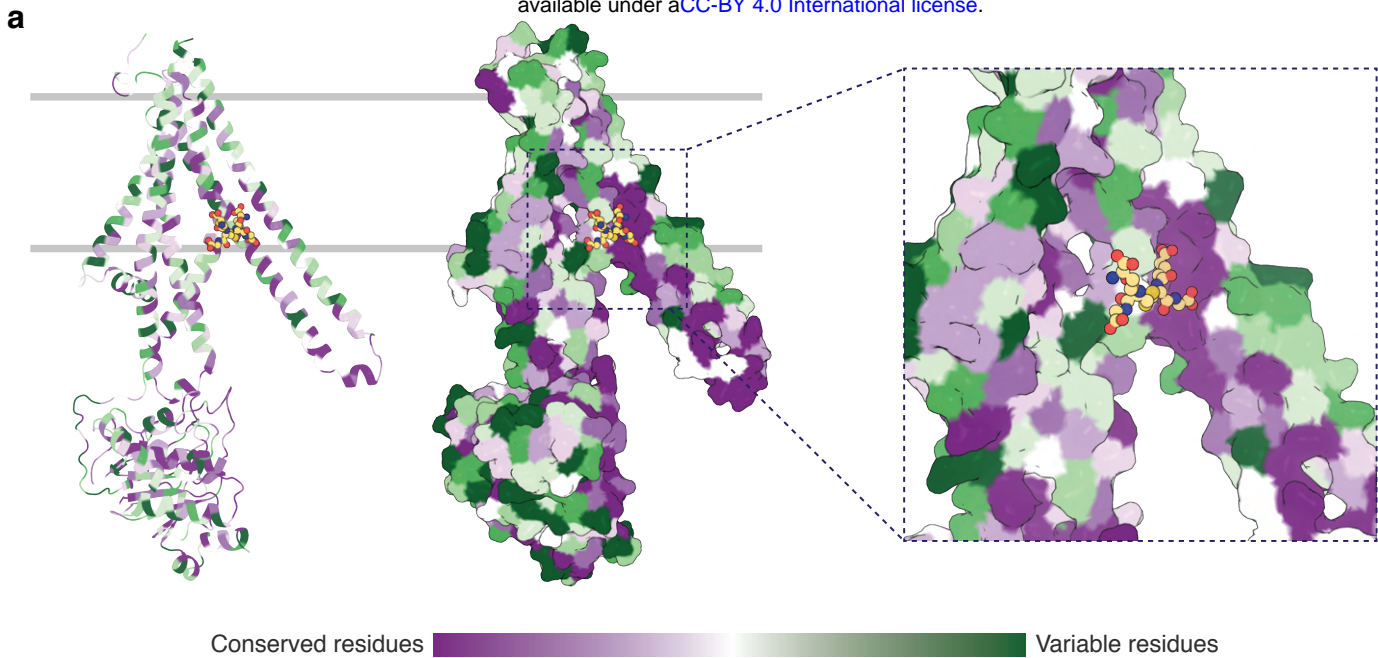


Figure 4. Substrate binding site conservation. **a)** Sequence conservation of *AtAtm3*, *NaAtm1*, *ScAtm1*, human ABCB7 and human ABCB6 calculated by ConSurf (Landau et al., 2005) plotted on a cartoon and surface representations of a half-transporter of *AtAtm3* in the GSSG bound inward-facing conformation. GSSG is shown in spheres. **b)** Conservation of key residues in the GSSG binding pocket. Residues in one chain is colored based on the conservation and residues in the second chain is colored in grey. All residues and GSSG are shown in ball and sticks.

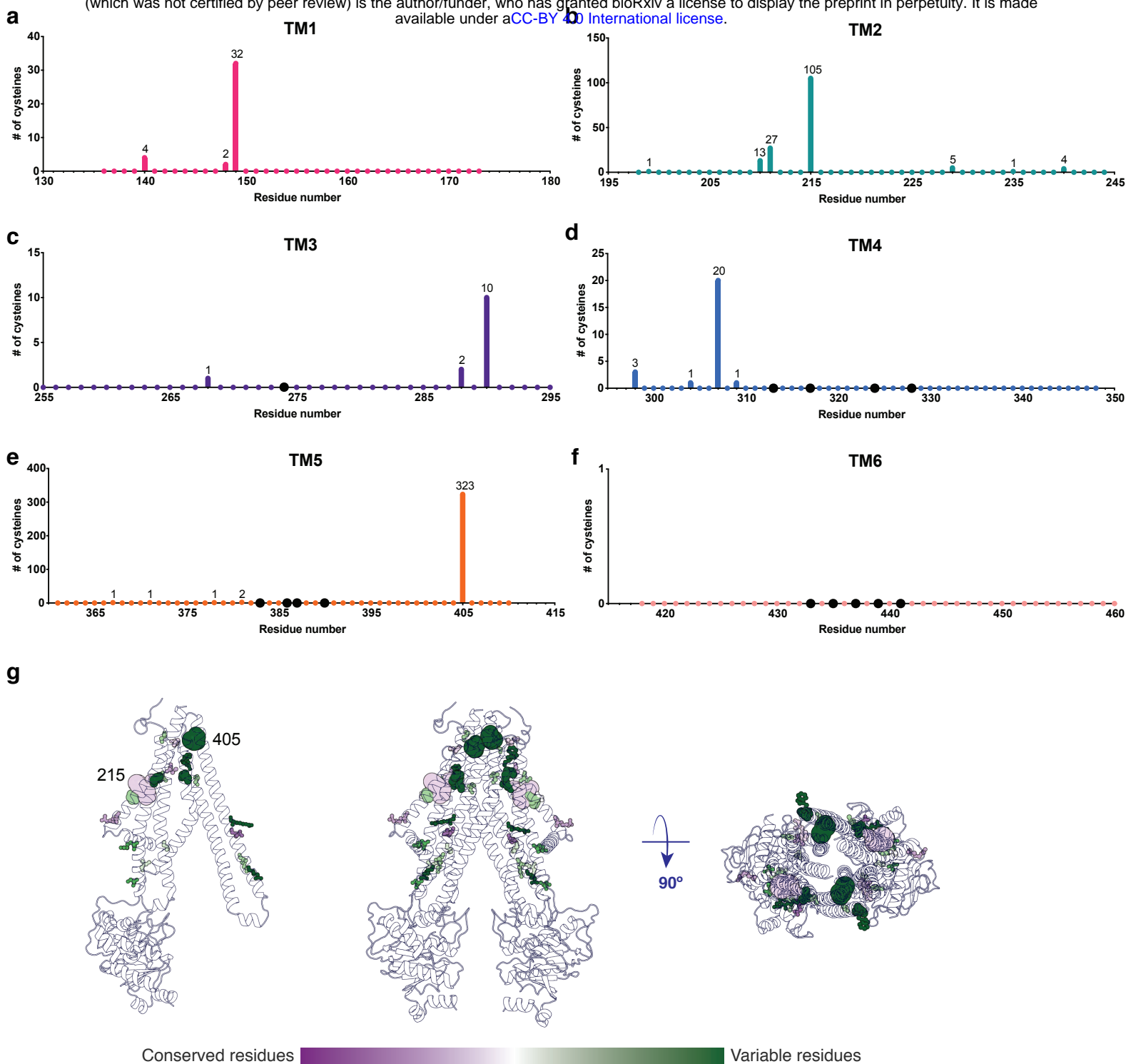


Figure 5. Cysteine residues found in transmembrane helices in an alignment of 410 *AtAtm3* homologs. a-f) Residues are numbered based on the *AtAtm3* sequence. Small colored dots represent different residue positions, while the larger black dots indicate residues observed to interact with glutathione in the *NaAtm1* and *AtAtm3* structures. The numbers above a given residue indicate the number of sequences in the alignment with a cysteine at that position; unlabeled positions denote positions where no cysteines were observed in the alignment. **g)** Transmembrane cysteine residues in the inward-facing conformation of *AtAtm3*. All positions with cysteine counts are shown in spheres. Positions that have 1 to 10 counts of cysteines are shown in small spheres, positions that have 11 to 100 counts of cysteines are shown in medium sized spheres, and positions with 101 and above counts of cysteines are shown in large spheres. The spheres are colored based on the consurf coloring in Figure 4. The distance between the $C\alpha$'s of two 215 residues is 37 Å, and the distance between the $C\alpha$'s of two 405 residues is 25 Å.

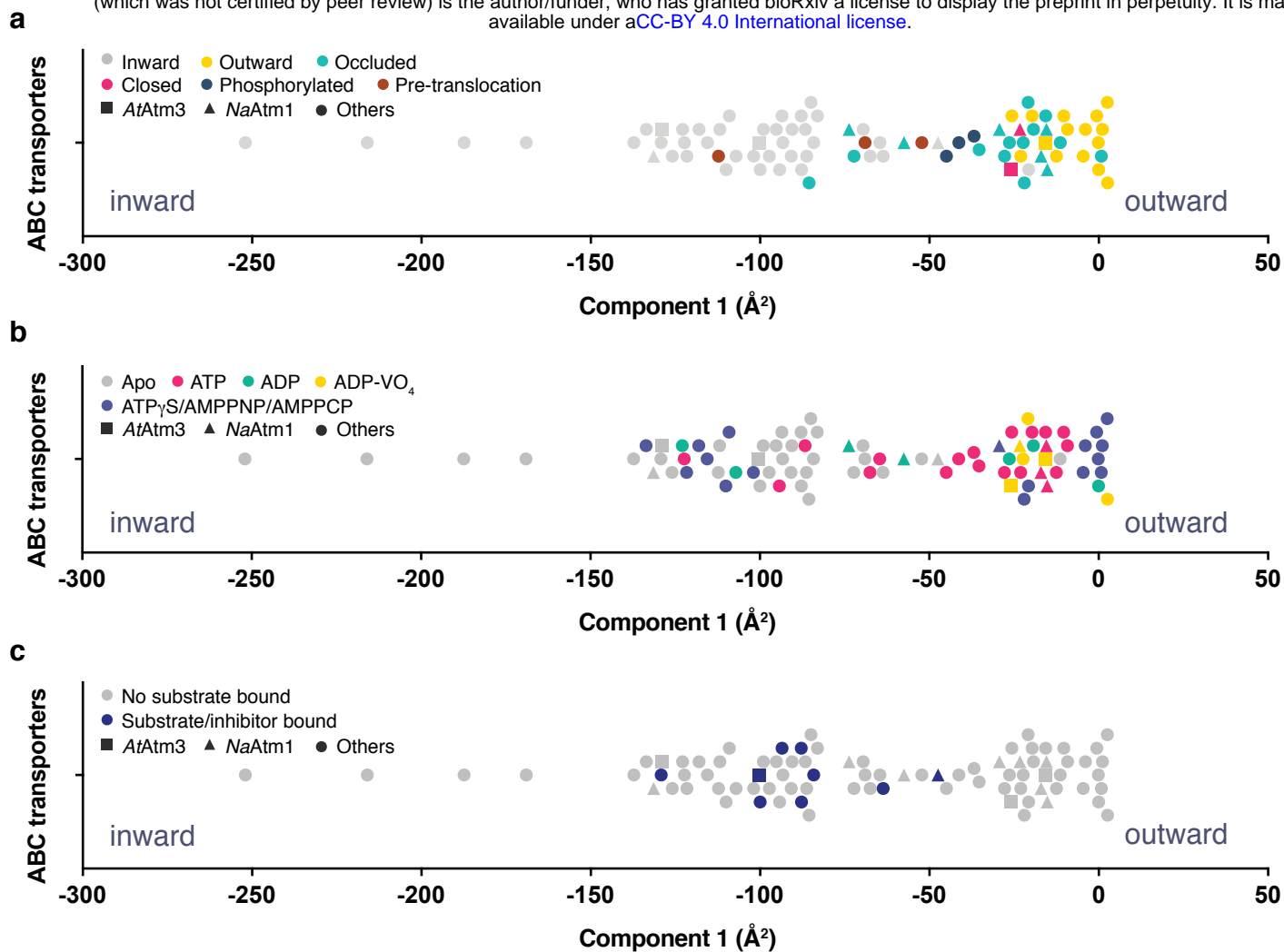


Figure 6. Principal component analysis (PCA) of type I ABC exporters. **a)** 1-dimensional plot of component 1, colored according to the conformational states assigned in the original publications. The plot is oriented with the most inward and most outward conformations to the left and right, respectively. **b)** 1-dimensional plot of component 1 with inward-facing to outward-facing structures, colored by their nucleotide states. **c)** 1-dimensional plot of component 1 with inward-facing to outward-facing structures, colored by their substrate states. Each marker (triangle (▲), square (■), circle (●)) represents a unique half-transporter structure. Triangles (▲) represent structures of *AtAtm3*, squares (■) represent structures of *NaAtm1* and circles (●) represent structures for other ABC transporters.

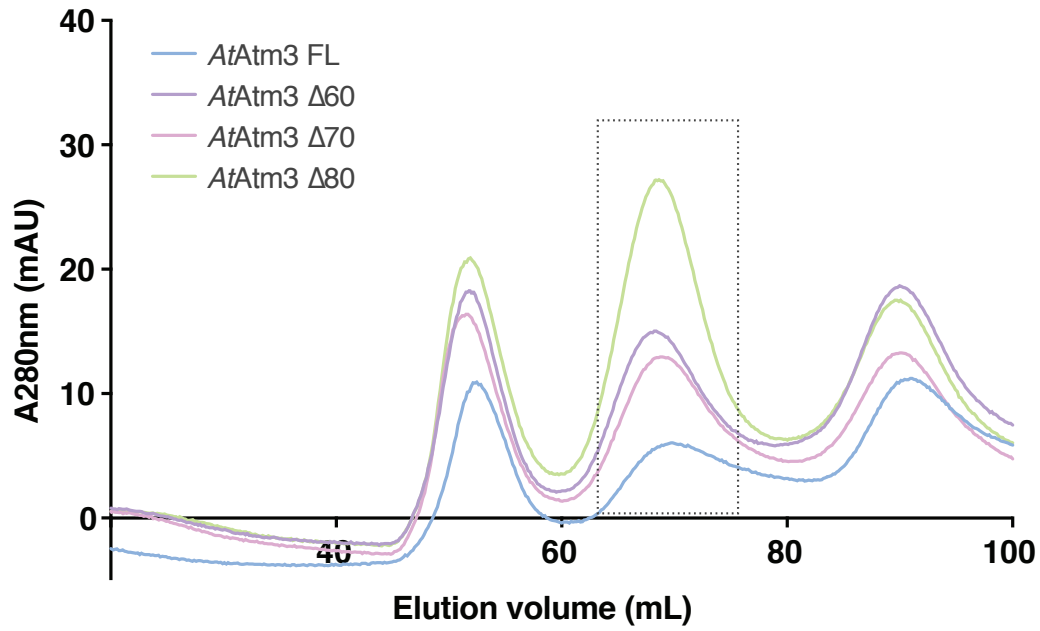


Figure S1. *AtAtm3* constructs. Size exclusion chromatography profile of *AtAtm3* constructs using HiLoad 16/60 Superdex 200 (GE Healthcare). Fractions collected for structural and functional analysis are boxed with dotted line.

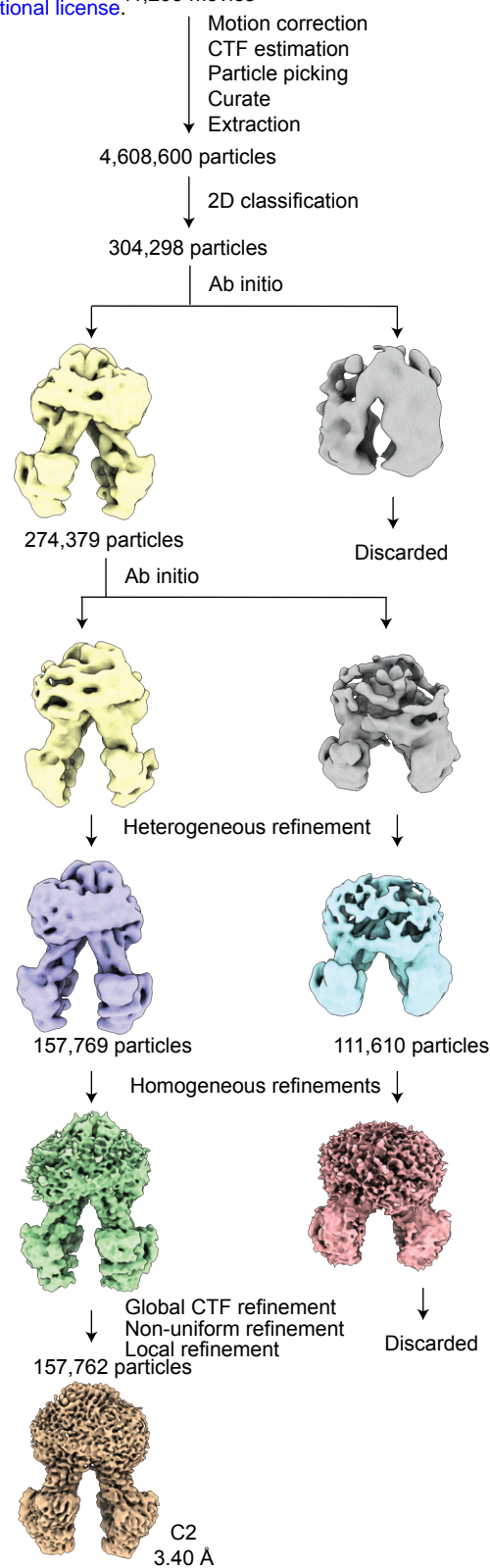
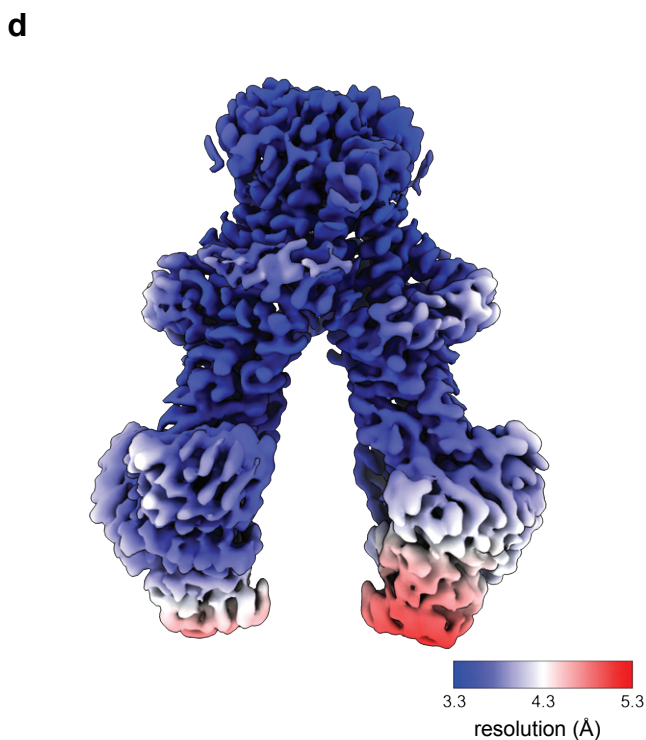
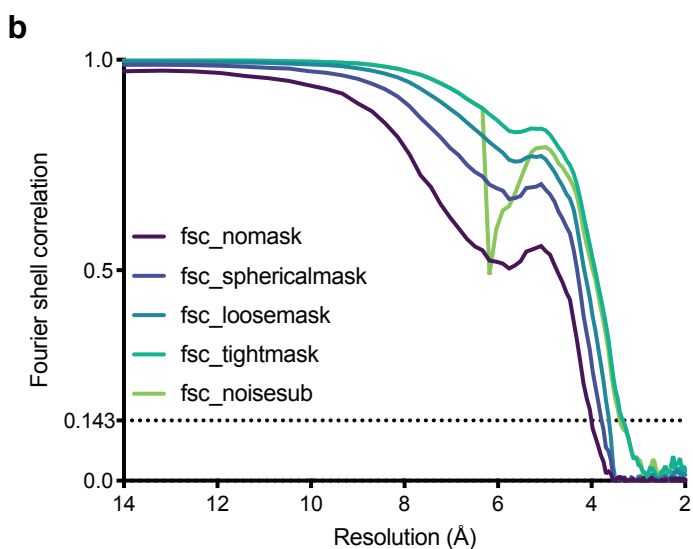
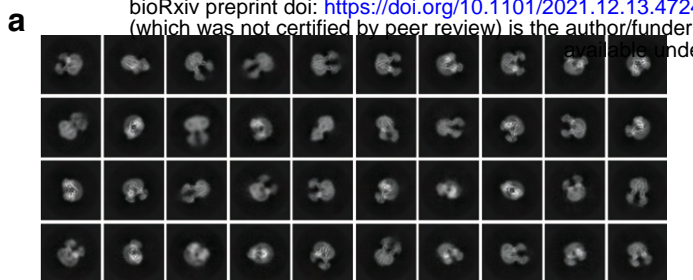


Figure S2. Single particle cryoEM structure of *AtAtm3* in the inward-facing conformation. a) Examples of 2D classes, **b)** FSC curves showing the resolution estimate for the final reconstruction, **c)** workflow of single-particle data processing, and **d)** local resolution estimation of the *AtAtm3* inward-facing conformation.

a

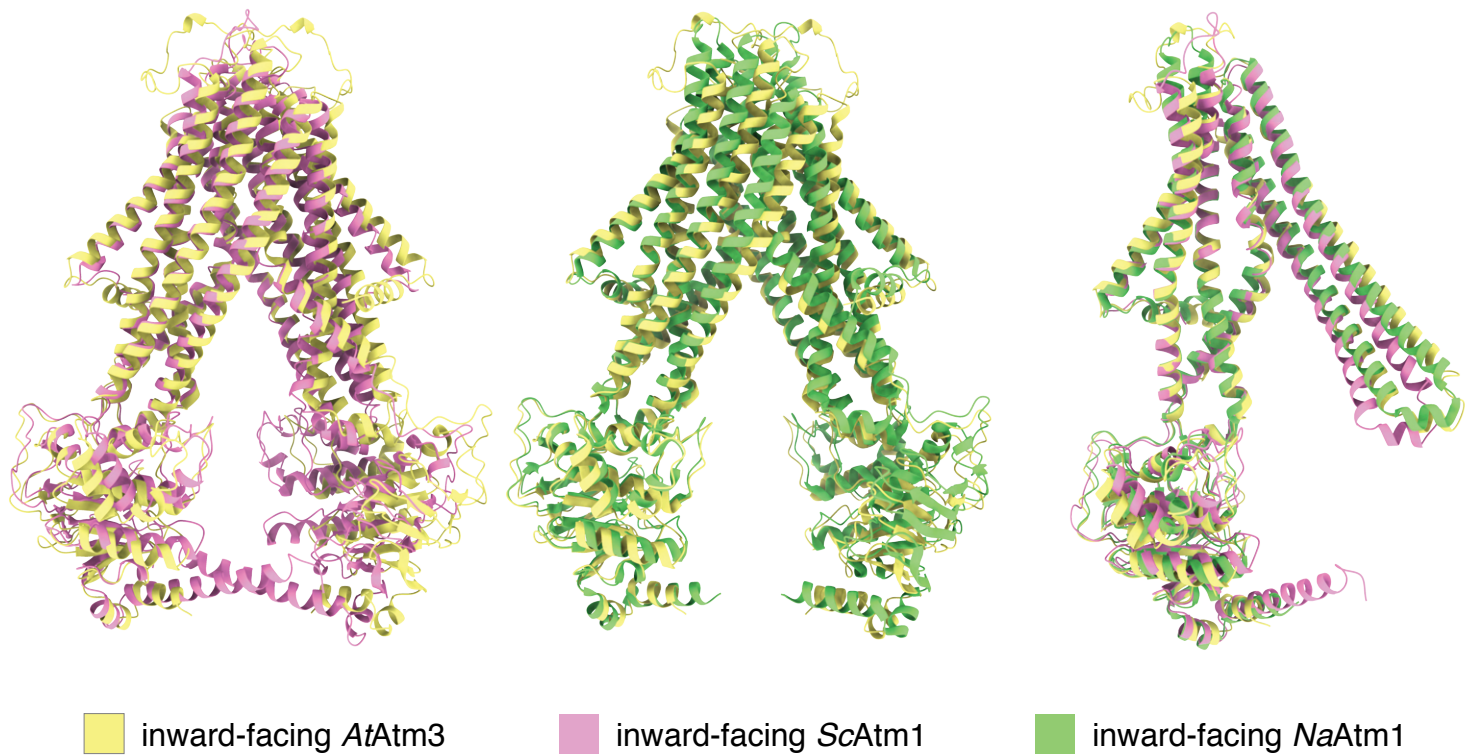


Figure S3. Structural alignment of *AtAtm3* to other ATM transporters. **a**) Overall alignment of inward-facing *AtAtm3* to *ScAtm1* (PDB ID: 4myc) with an overall RMSD of 2.6 Å. **b**) Overall alignment of inward-facing *AtAtm3* to *NaAtm1* (PDB ID: 6vqu) with an overall RMSD of 2.1 Å. **c**) Half-transporter alignments *ScAtm1* (PDB ID: 4MYC) and *NaAtm1* (PDB ID: 6vqu) to inward-facing *AtAtm3* to with RMSDs of 2.3 Å and 2.0 Å, separately.

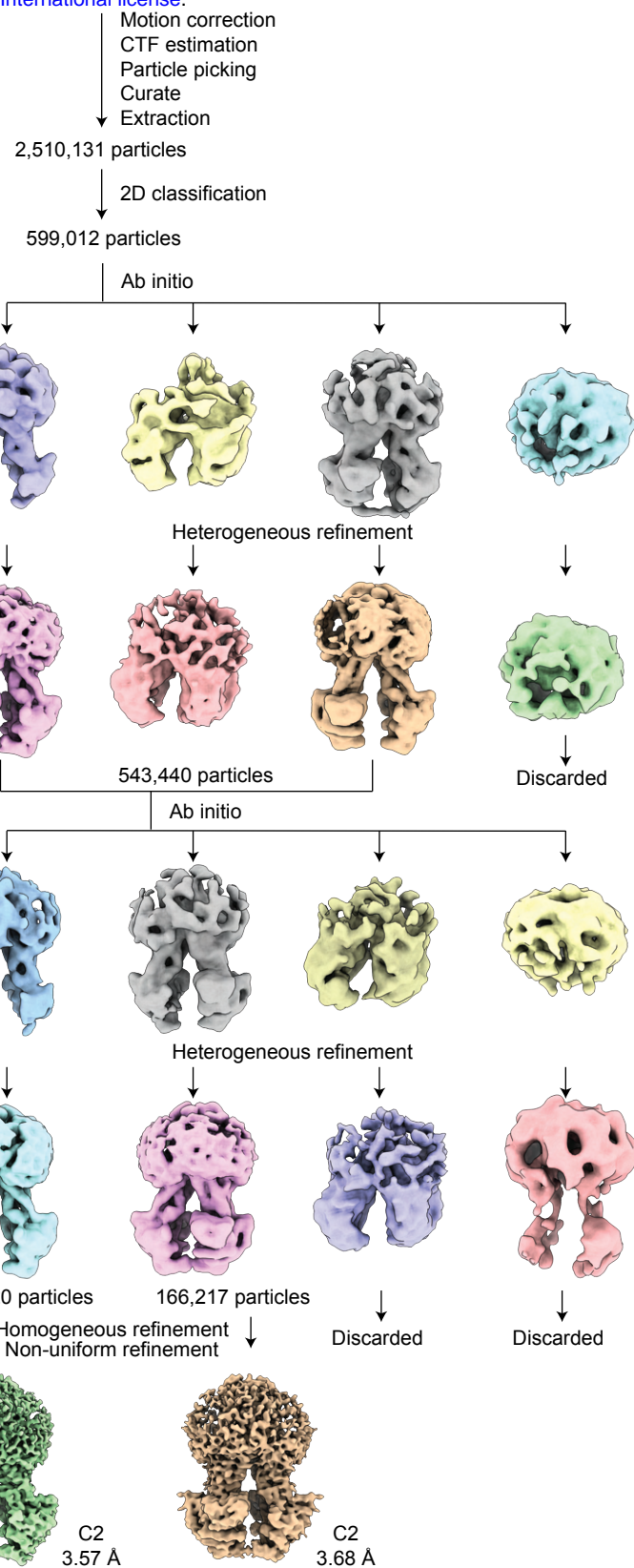
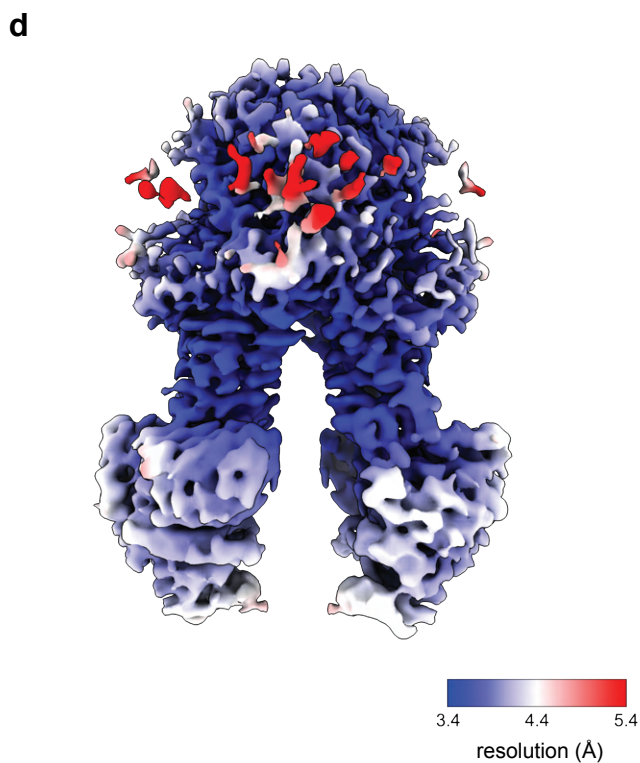
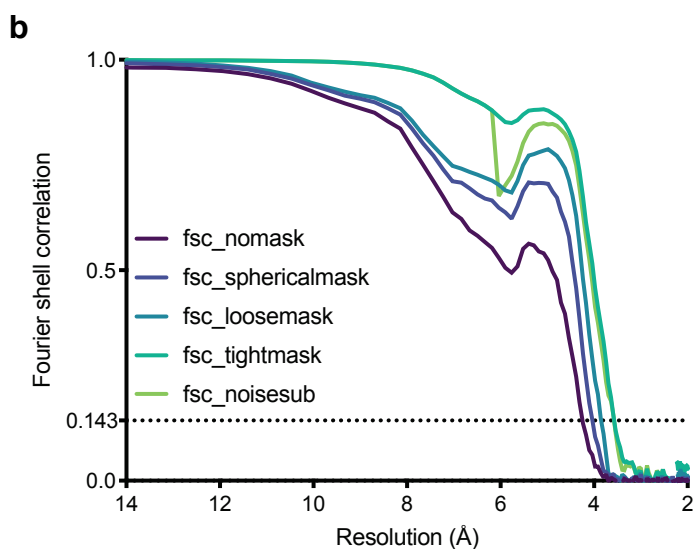
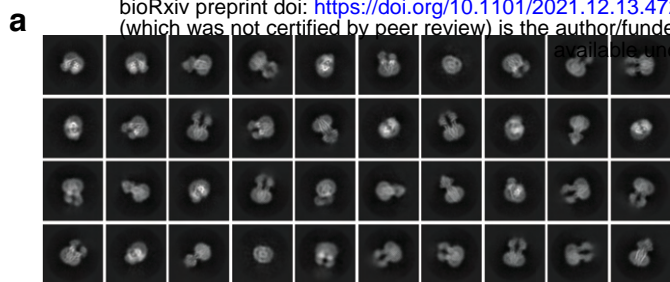
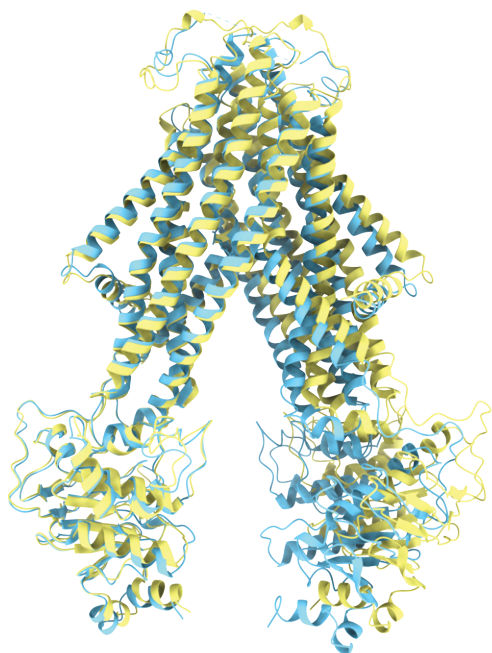


Figure S4. Single particle cryoEM structure of *AtAtm3* in the inward-facing conformation with GSSG bound. **a)** Examples of 2D classes, **b)** FSC curves showing the resolution estimate for the final reconstruction, **c)** workflow of single-particle data processing, and **d)** local resolution estimation of the *AtAtm3* inward-facing conformation with GSSG bound.

a



 inward-facing *AtAtm3*

 inward-facing *AtAtm3* with GSSG

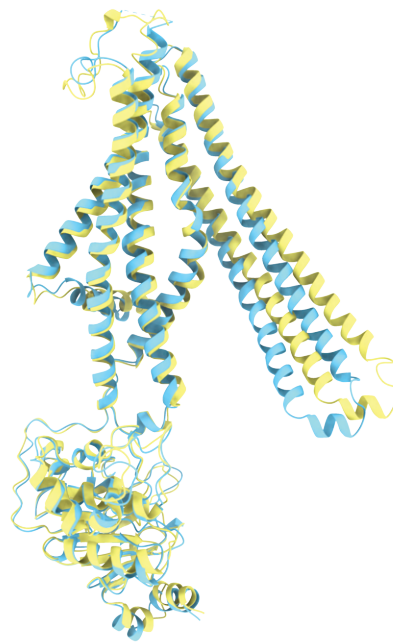


Figure S5. Structural alignment of *AtAtm3* in the inward-facing conformation. a) Overall alignment of inward-facing *AtAtm3* in the apo state to the GSSG bound state with an overall RMSD of 2.9 Å. **b)** Half-transporter alignment inward-facing *AtAtm3* in the apo state to the GSSG bound state with an RMSD of 1.6 Å.

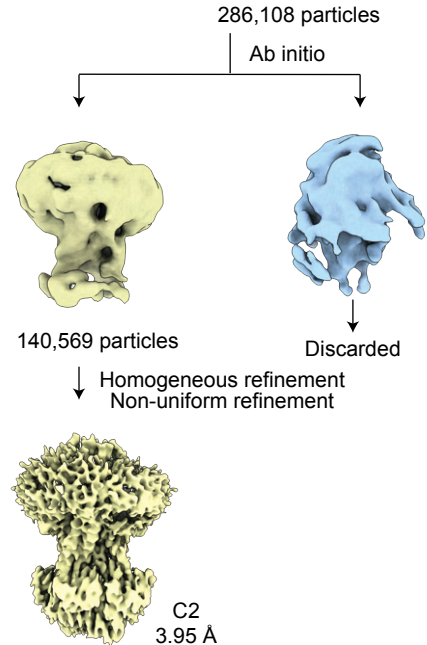
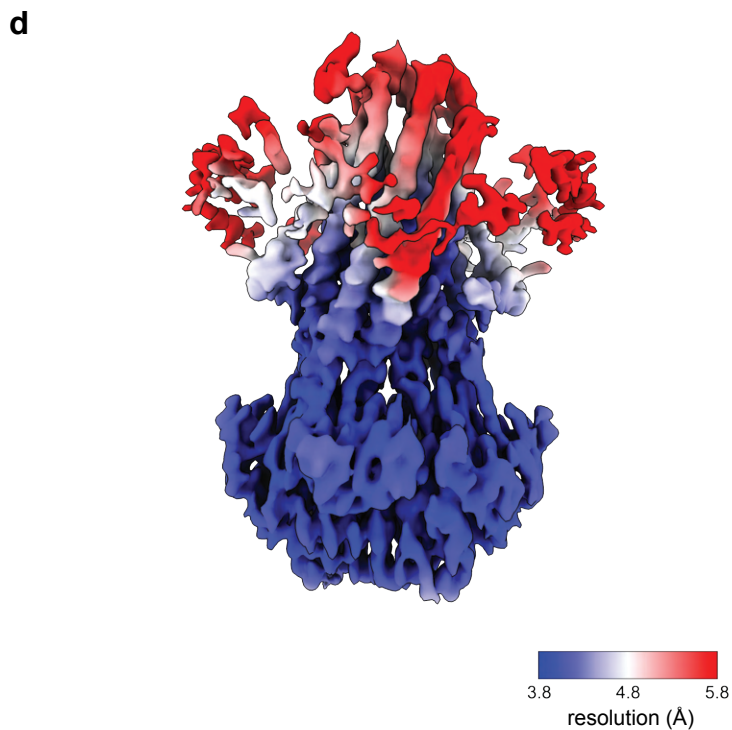
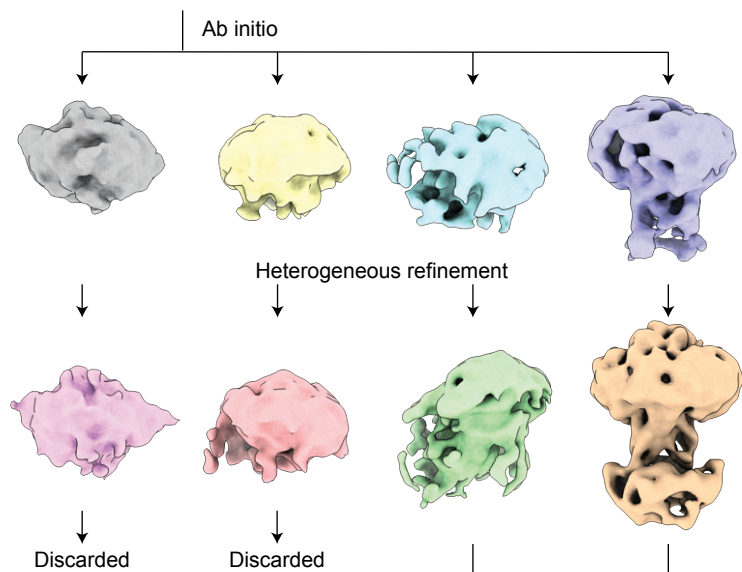
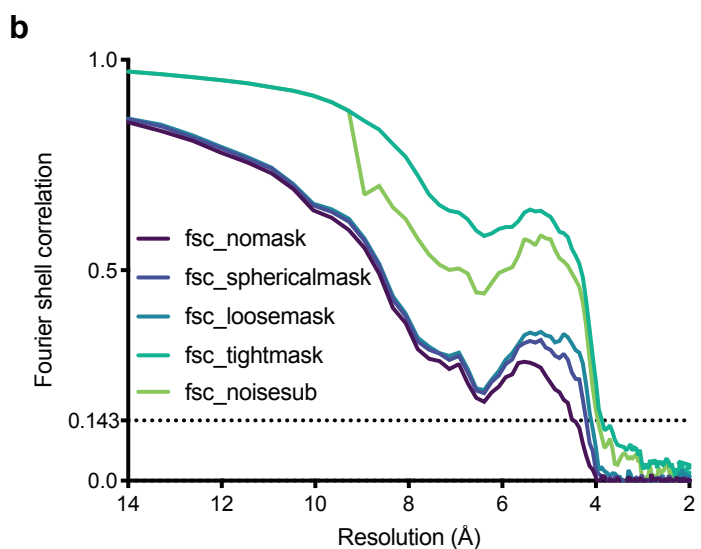
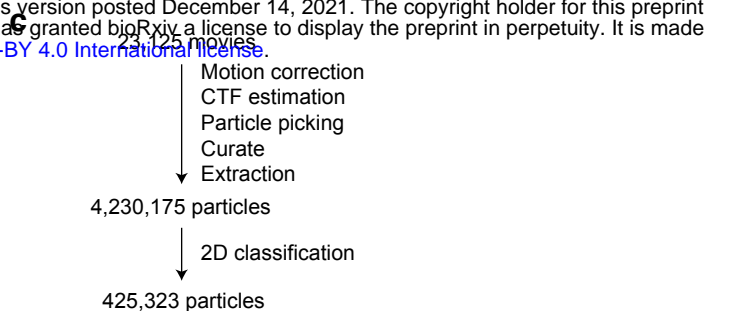
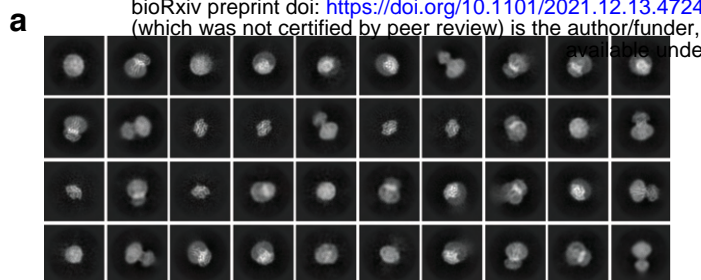


Figure S6. Single particle cryoEM structure of *AtAtm3* in the closed conformation. a) Examples of 2D classes, **b)** FSC curves showing the resolution estimate for the final reconstruction, **c)** workflow of single-particle data processing, and **d)** local resolution estimation of the *AtAtm3* closed conformation.

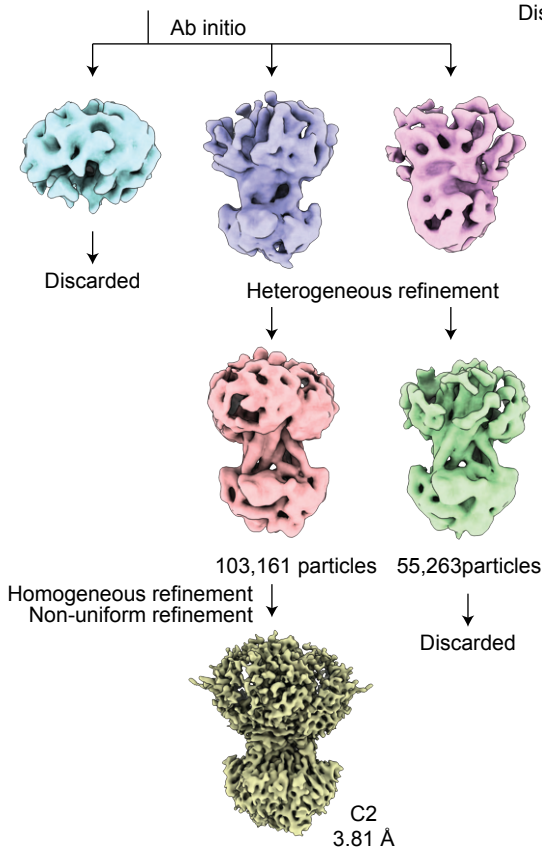
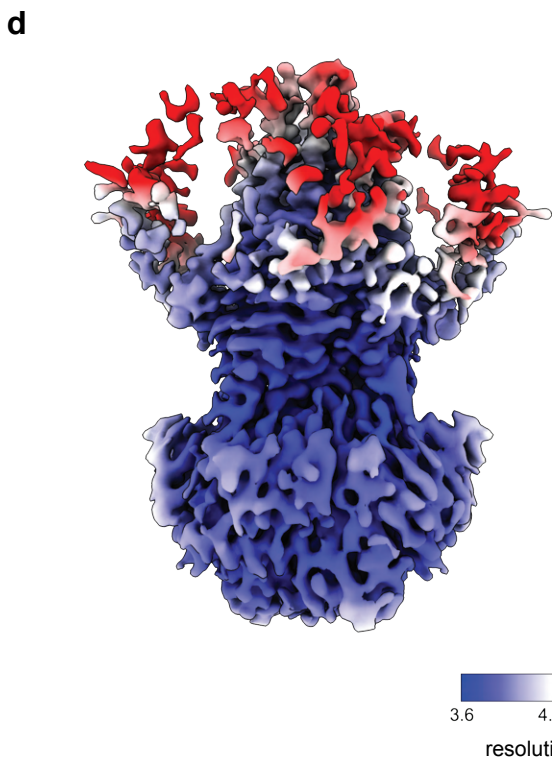
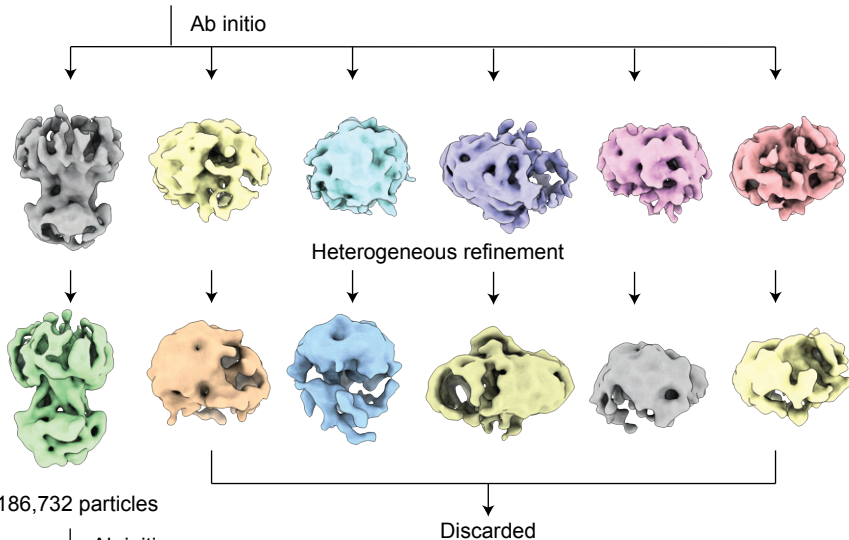
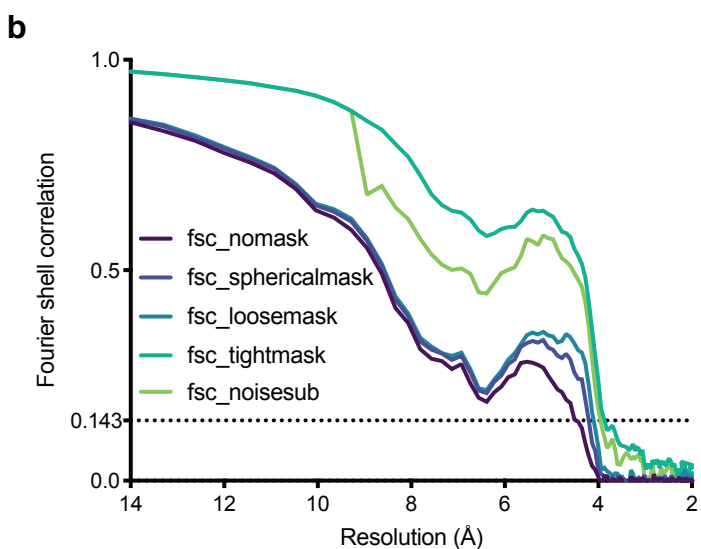
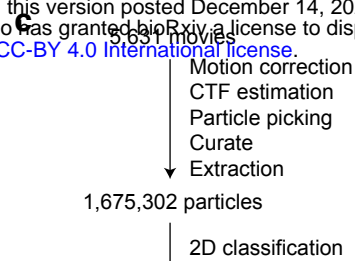
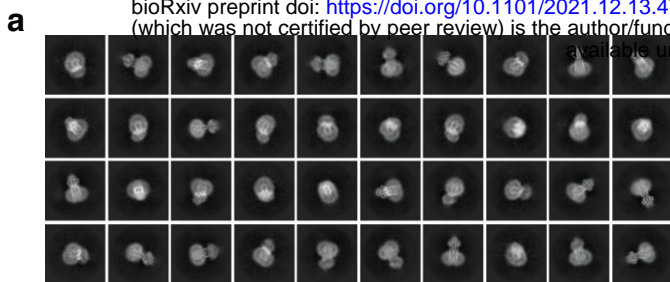


Figure S7. Single particle cryoEM structures of *AtAtm3* in the outward-facing conformation. a) Examples of 2D classes, **b)** FSC curves showing the resolution estimate for the final reconstruction, and **c)** workflow of single-particle data processing, and **d)** local resolution estimation of the *AtAtm3* outward-facing conformation.

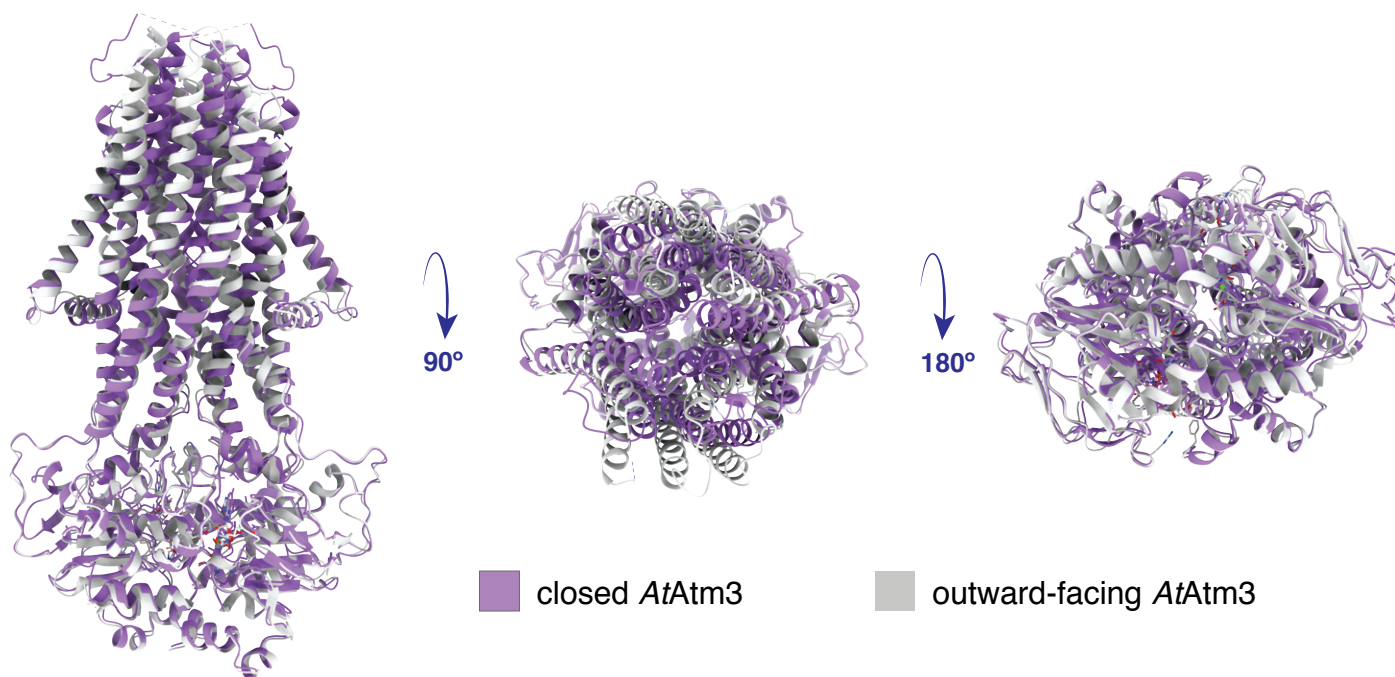


Figure S8. Structural alignment of *AtAtm3* in the closed and outward-facing conformation. Overall alignment of *AtAtm3* in the closed and outward-facing conformation with an overall RMSD of 1.7 Å.

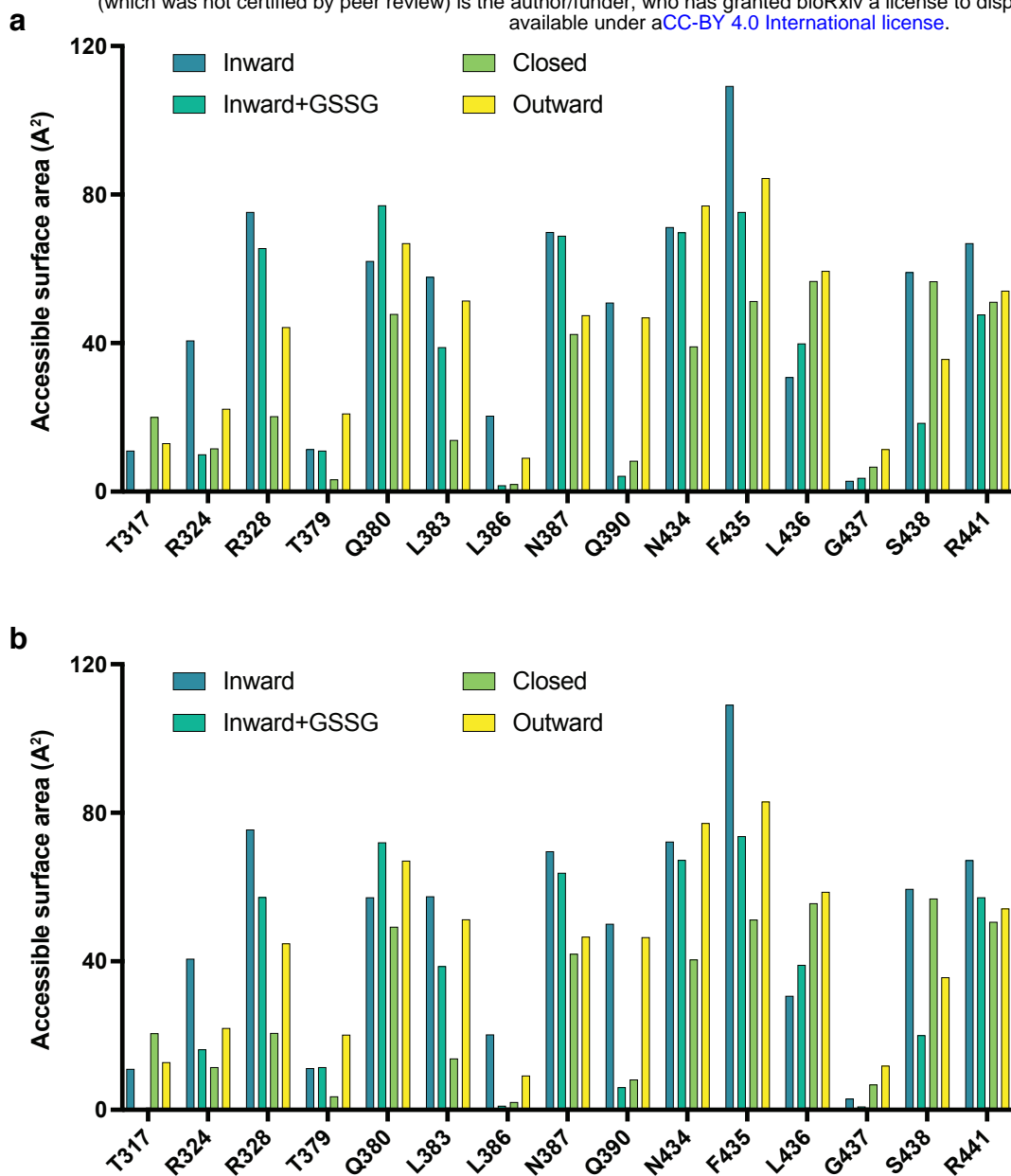


Figure S9. Accessible surface area of binding site residues. Accessible surface area for GSSG binding pocket residues in **a**) chain A and **b**) chain B, calculated by Areaimol in CCP4 (Winn et al.2011).

AtAtm3 1
NaAtm1 1
ScAtm1 1
ABCB7 1
ABCB6 1 **MVTVGN YCEAEGPVGPAWMQDGLSPCFFFTLPSTRMALGTLALV LALPCRRRER PAGADSLSWGAGPRI**

AtAtm3 1 **MSRGRS R FVRAPG LLLCRVNLQPQPKIPS**
NaAtm1 1
ScAtm1 1 **MLL**
ABCB7 1 **MALLAMHS**
ABCB6 71 **SPYVLQ LLLATLQAALPLAGLAGRVGTARGAPLPSYLLLASVLES LAGACGLWLLVVERS QARQLAMGI**

AtAtm3 29 **FSYSLRSDYRLHNGFSNYIRRNSIRTS PVINAF LSDNS . . . PSPSPSPSPIRFVQRSSMLNGRLFSTSTP**
NaAtm1 1 **M**
ScAtm1 4 **LPRCPVIGRIVRSKFRSGLIRNHSPVIFTVSKLSTQRP . . . LLFNSAVNLWNQAOK . DITHKKSVEQFSS**
ABCB7 9 **WRWAAAAAAFEKRRHSAILIRPLVSVSGSPQWRPHQL . . . GALG . TARAYQALQVWPLIEKRTCWHGHA**
ABCB6 141 **WIKFRHSPGLLLLWTVAFAAENLALVSWNSPQWWWARADLGQQVQFSLWVLRVYVSVGGFLVGLWAPGLR**

TM1

AtAtm3 96 **NPDQTTTKTKEIKTSSDSDSAMADM KILRTL AGLYLMWRDNPEFRFRVIAALGFLV GAKVLNV**
NaAtm1 2 **PPETATNPKDARHDGWQT LKRFLPYLW PADNAVLRRRVGAILMVL L GKATTL**
ScAtm1 70 **APKVKTVQVKKTSKAPTLS EL KILKDLFRYIWPKGNNKVRIRVLI ALGLLISAKI LNV**
ABCB7 75 **GGGLHTDPKEGLKDVDR KIIKAMLSYVWPKDRPDLRVAI SLGFLGGAKAMNI**
ABCB6 211 **PQSYTLQVHEEDQDVERSQVRSAAQQSTWRDFGRKLRLLSGYLWPRGSPALQLVVLICLGLMGLERALNV**

TM1 **TM2**

AtAtm3 159 **QVPFLFKLAVDWLASATGT . GASLTTF AATNP TLLTVFATPAAVLIGYGIARTGSSAFNELRTAVFSKVA**
NaAtm1 55 **ALPFAYKKAVDAMTLGGGA . QPALT VALAFVLAYALGRFSGVLF DNLRNIVFERVG**
ScAtm1 127 **QVPFFFKQTIDSMNIAWDDPTVALP AAIGLTI L CYGVARFGSVLFGELRNAVFAKVA**
ABCB7 130 **VVPFMFKYAVDSL NQMSGN . MLNLS . . DAPN . . . TVATMATAVLIGYGVSRAGAA FNEVRNAVFGKVA**
ABCB6 281 **LVPIFYRNI VNL L TEKAPWNSLAWT VTSYVFLKFLQGGGTGSTGFVSNLRTFLWIRVQ**

TM2 **TM3**

AtAtm3 228 **LRTIRSVSRKVFSHLHDLDRYHLSRETGG LNRIIDRGSRAINFI L SAMVFNVP T ILEISMVSGI LAYK**
NaAtm1 110 **QDATHRLAENVFARLHKLSLRFHLARRTGEVTKVIERGTKSIDT MLYFLLFNIAPTVIELTAVIVIFWLN**
ScAtm1 184 **QNAIRTVSLQTFQHLMKLDLGWHL SRQTGG LTRAMDRGTKGISQVLTAMVFHIIPI SFEISVVCGILTYQ**
ABCB7 193 **QNSIRRIAKNVFLHLHNL D LGFHL SRQTGALS KAIDRGTRGISFVLSALVFNLLPIMFEVMLVSGVLYYK**
ABCB6 339 **QFTSRREVELLIFSHLHEL SLRWHLGRRTGEVLR IADRGTSSVTGLLSYL VFNVIPTLADIIIGIIFYSMF**

TM4 **TM5**

AtAtm3 298 **FGAAFAWITSLVGSYIVFTLAVTQWR TKFRKAMNKADNDASTRAIDSLIN YETVKYFNNEGYEAEKYDQ**
NaAtm1 180 **FGLGLVTATILAVIAYVWTRTITIEWRTHLREKMNRLDGOALARA VDSL LNYETVKYFGAESREEARYAS**
ScAtm1 254 **FGASFAAITFSTMLLYSIFTIKTTAWRTHFRRDANKADNKAASVALDSLINF EAVKYFNNEKYLADKYNG**
ABCB7 263 **CGAQFALVTLGTLGTYTAFTVAVTRWRTRFRIEMNKADNDAGNA AIDSL LNYETVKYFNNERIEAQRYDG**
ABCB6 409 **FNAWFGLIVFLCMSLYLTLTIVVTEWR TKFRAMNTQENATRARA VDSL LNFETVKYNAESYEVERYRE**

TM5 **TM6**

AtAtm3 368 **FLKKYEDAALQ TQ RSLAFLNFGQS IIFSTALSTAMV LCSQGIMNGQMTVGD LVMVNGLLFQLS LPLNFLG**
NaAtm1 250 **AARAYADA AVKSENSLGLLNIAQALIVNLLMAGAMA WTVYGWSQGKLT VGD L VFNTYLTQLFRPLDMLG**
ScAtm1 324 **SLMNYRDSQIKVSQSLAFLNSGQNLIFTTALTAMMYMGCTGVIGGNLTVGD LVLINQLV FQLS VPLNFLG**
ABCB7 333 **FLKTYETASLKSTSTLAMLNFGQSAIFSVGLTAIMV LASQGIVAGTLTVGD LVMVNGLLFQLS LPLNFLG**
ABCB6 479 **AI IKYQGLEWKSSASLVLLNQTQNLVIGLGLLAGSLLCAYFVTEQKLQVGDYVLFGTYI IQLYMPLNWF**



Figure S10. Sequence alignments of selected Atm family transporters. Sequence alignment generated by was generated using STRAP (<http://www.bioinformatics.org/strap/>). *At*: *Arabidopsis thaliana*; *Na*: *Novosphingobium aromaticivorans* and *Sc*: *Saccharomyces cerevisiae* (yeast). ABCB7 and ABCB6 are human ABC transporters. Positions of the six transmembrane helices are indicated above the sequence alignment. The key residues interacting with GSSG or GSH are highlighted in yellow. The substrate interacting residues are identified based on the structures of GSSG-bound *NaAtm1* (PDB ID: 4mrs) and *AtAtm3* (PDB ID: 7n59), and the GSH-bound structure of *ScAtm1* (PDB ID: 4myh).

Table S1. Cryo-EM data collection, refinement and validation statistics

	Inward	Inward + GSSG	Closed	Outward
Data Collection and processing				
Microscope	Titan Krios at Caltech Cryo-EM facility	Titan Krios at Caltech Cryo-EM facility	Titan Krios at Stanford-SLAC CryoEM Center (S2C2)	Titan Krios at Caltech Cryo-EM facility
Camera	Gatan K3	Gatan K3	Falcon IV	Gatan K3
Magnification	x105,000	x105,000	-	x105,000
Voltage (keV)	300	300	300	300
Exposure (e/Å ²)	60	60	48	60
Pixel size (Å)	0.855	0.855	0.82	0.855
Defocus Range (um)	- 1.0 to -3.0	- 1.0 to -3.0	- 1.5 to -2.1	- 1.0 to -3.0
Initial Particle Image (no.)	4,608,600	2,510,131	4,230,175	1,675,302
Final Particle Image (no.)	157,762	259,020	140,569	103,161
Symmetry Imposed	C2	C2	C2	C2
Map Resolution (Å)	3.4	3.6	4.0	3.8
FSC Threshold	0.143	0.143	0.143	0.143
Map Resolution Range (Å)	3.2 - 4.1	3.5 - 4.0	3.9 - 4.2	3.9 - 4.3
Refinement				
Initial Model Used	PDB ID: 6pam	PDB ID: 6pam	PDB ID: 6par	PDB ID: 6par
Model Resolution (Å)	3.4	3.57	3.95	3.81
FSC Threshold	0.143	0.143	0.143	0.143
Model composition				
non-hydrogen atoms	9,326	9,238	9,254	9,122
protein residues	1,200	1,180	1,178	1,160
ligands	-	GDS:1	ADP: 2; MG: 2; VO ₄ :2	ADP: 2; MG: 2; VO ₄ :2
Average B-factors (Å²)				
protein	99.8	76.5	118.7	49.3
ligands	-	34.3	62.1	25.3
R.m.s. deviations				
Bond length (Å)	0.004	0.002	0.003	0.002
Bond angles (°)	0.841	0.562	0.613	0.482
Validation				
MolProbity score	1.82	1.41	1.60	1.41
Clashscore	14.6	6.9	11.8	6.3
Rotamer outliers	0	0.1	0.2	0.2
Ramachandran plot				
Ramachandran favored (%)	97.2	97.9	98.0	97.7
Ramachandran allowed (%)	2.8	2.1	2.1	2.3
Ramachandran outliers (%)	0	0	0	0
PDB ID	7n58	7n59	7n5a	7n5b

PDB ID	Component 1 (A ²)	PDB ID	Component 1 (A ²)
2hyd	0	5uj9_B	-93.27
3b5w	-252.01	5uja_A	-87.87
3b5x	-95.19	5uja_B	-63.67
3b5y	-0.09	5w81_A	-41.29
3b5z	2.61	5w81_B	-45
3b60	-0.59	6bhu_A	-25.63
3g5u_A	-112.24	6bhu_B	-23.02
3g5u_B	-52.24	6bpl	-84.93
3qf4_A	-115.57	6c0v_A	-10.35
3qf4_B	-109.08	6c0v_B	-19.67
3wme	-90.79	6fn4_A	-85.55
3zdq	-125.91	6fn4_B	-72.26
4ayt	-117.99	6hrc	0.8
4ayw	-121.61	6msm	-36.8
4ayx	-133.59	6qee_A	-87.78
4f4c	-168.99	6qee_B	-84.19
4mrs	-47.43	6quz_A	-4.53
4myc	-111.84	6quz_B	2.57
4pl0	-21.98	6qv2_A	-3.93
4q4a_A	-101.87	6qv2_B	1.11
4q4a_B	-110.01	6raf_A	-86.61
4ry2	-68.98	6raf_B	-64.64
5c73	-19.25	6rag_A	-107.09
5c76	-187.37	6rag_B	-94.21
5c78	-215.98	6rah_A	-9.19
5eg1	-20.71	6rah_B	-12.44
5koy_A	-122.35	6rai_A	-15.64
5koy_B	-67.46	6rai_B	-27.8
5mkk_A	-97.26	6ral_A	-26.39
5mkk_B	-99	6ral_B	-35.32
5nbd	-122.85	6pam_A	-57.51
5ofp	-11.32	6pam_B	-73.71
5ofr	-20.86	6pan	-15.17
5ttp	-22.3	6pao	-17.01
5tv4	-99.97	6paq	-15.42
5u1d_A	-129.2	6par	-29.28
5u1d_B	-93.49	6vqu	-131.4
5uak_A	-90.58	6vqt	-23.27
5uak_B	-83.07	7n58	-128.9
5uar_A	-86.26	7n59	-100.4
5uar_B	-69.55	7n5a	-25.82
5uj9_A	-137.22	7n5b	-15.71

Table S2. Principal component analysis. Calculated component 1 values are listed for different transporters. For heterologous transporters, transporter encoded in one polypeptide and transporters with different conformational states in one PDB file, “_A/B” is added at the end of each PDB to represent different half-transporters and/or different conformations.